PHYSICAL REVIEW C **73**, 044904 (2006)

Relativistic heavy-ion collisions within three-fluid hydrodynamics*: Hadronic scenario

Yu. B. Ivanov,[1,2,†] V. N. Russkikh,[1,2,‡] and V. D. Toneev[1,3,§]
[1]*Gesellschaft für Schwerionenforschung mbH, Planckstraße 1, D-64291 Darmstadt, Germany*
[2]*Kurchatov Institute, Kurchatov sq. 1, RU-123182 Moscow, Russia*
[3]*Joint Institute for Nuclear Research, RU-141980 Dubna, Moscow Region, Russia*

(Received 1 April 2005; published 19 April 2006)

A three-fluid hydrodynamic model for simulating relativistic heavy-ion collisions is introduced. Along with two baryon-rich fluids, the new model considers the time-delayed evolution of a third, baryon-free (i.e., with zero net baryonic charge) fluid of newly produced particles. Its evolution is delayed because of a formation time τ, during which the baryon-free fluid neither thermalizes nor interacts with the baryon-rich fluids. After the formation it starts to interact with the baryon-rich fluids and quickly gets thermalized. Within this model with pure hadronic equation of state, a systematic analysis of various observables at incident energies between few and about 160*A* GeV has been done as well as a comparison with results of transport models. We have succeeded in reasonably reproducing a great body of experimental data in the incident energy range of $E_{\text{lab}} \simeq (1\text{–}160)A$ GeV. The list includes proton and pion rapidity distributions, proton transverse-mass spectra, rapidity distributions of Λ and $\bar{\Lambda}$ hyperons, elliptic flow of protons and pions (with the exception of proton v_2 at 40*A* GeV), multiplicities of pions, positive kaons, ϕ mesons, hyperons, and antihyperons, including multistrange particles. This agreement is achieved on the expense of substantial enhancement of the interflow friction as compared to that estimated proceeding from hadronic free cross sections. However, we have also found out certain problems. The calculated yield of K^- is approximately higher than that in the experiment by a factor of 1.5. We have also failed to describe directed transverse flow of protons and pion at $E_{\text{lab}} \geqslant 40A$ GeV. This failure apparently indicates that the used EOS is too hard and thereby leaves room for a phase transition.

DOI: 10.1103/PhysRevC.73.044904 PACS number(s): 24.10.Nz, 25.75.−q

I. INTRODUCTION

Relativistic nucleus-nucleus collisions at incident energies $E_{\text{lab}} \simeq (10\text{–}40)A$ GeV presently attracts special attention, because the highest baryon densities [1,2] and highest relative strangeness [3] at moderate temperatures are expected in this incident energy range. The interest to this energy range has been recently also revived in connection with new experimental results from low-energy scanning SPS program [4] and the project of the new accelerator facility SIS300 at GSI [5]. This domain of the nuclear phase diagram is less explored both experimentally and theoretically as compared to the corresponding extremes, i.e., cold compressed matter and baryon-free hot matter. Moreover, a critical point of the quantum chromodynamics (QCD) phase diagram may occur to be accessible in these reactions [6,7]. There are already available experimental data [4] pointing out that something interesting really happens in this energy range. To draw information on properties of hot and compressed nuclear matter from available experimental data, we need better understanding of dynamics of nucleus-nucleus collisions under investigation.

A direct way to address thermodynamic properties of the matter produced in these reactions consists in application of hydrodynamic simulations to nuclear collisions. However, finite nuclear stopping power, revealing itself at high incident energies, makes the collision dynamics nonequilibrium and prevents us from application of conventional hydrodynamics especially at the initial stage of the reaction. Because the resulting nonequilibrium is quite strong, introduction of viscosity and thermal conductivity does not help to overcome this difficulty, because by definition they are suitable for weak nonequilibrium. A possible way out is taking advantage of a multifluid approximation to heavy-ion collisions, pioneered by Los Alamos group [8,9] and further developed at the Kurchatov Institute [10–12], Frankfurt [13–15], and GSI [16,17]. The last development [16,17], i.e., the mean-field dynamics in the multifluid background, concerns mostly moderate energies around 1 GeV/nucleon and therefore is not discussed here.

The first extension of the original two-fluid model [8,9], the two-fluid hydrodynamics with free-streaming radiation of pions, was advanced in Ref. [10]. The initial stage of heavy-ion collisions definitely is a highly nonequilibrium process. Within the hydrodynamic approach this nonequilibrium is simulated by means of a two-fluid approximation, which takes care of the finite stopping power of nuclear matter [18,19] and simultaneously describes the entropy generation at the initial stage. The radiated pions form a baryon-free matter in the midrapidity region, whereas two baryon-rich fluids simulate the propagation of leading particles. The pions are the most abundant species of the baryon-free matter that may contain any hadronic, including baryon-antibaryon pairs and/or quark-gluon species.

First applications of the two-fluid model with direct pion radiation [11,12] were quite successful for describing heavy-ion collisions in the wide range of incident energies, from SIS to SPS. In these 3D hydrodynamic simulations the whole

---

*http://theory.gsi.de/∼mfd/

[†] Electronic address: Y.Ivanov@gsi.de

[‡] Electronic address: russ@ru.net

[§] Electronic address: V.Toneev@gsi.de

process of the reaction was described, i.e., the evolution from the formation of a hot and dense nuclear system to its subsequent decay. This is in distinction to numerous other simulations, which treat only the expansion stage of a fireball formed in the course of the reaction, whereas the initial state of this dense and hot nuclear system is constructed from either kinetic simulations [20] or more general albeit model-dependent assumptions (e.g., see Refs. [21,22]).

However, the approximation of free-streaming pions, produced in the midrapidity region, was still irritating from the theoretical point of view, in particular, because the relative momenta of the produced pions and the leading baryons are in the range of the Δ resonance for the incident energies considered. This would imply that the interaction between the produced pions and the baryon-rich fluids should be strong. The free-streaming assumption relies on a long formation time of produced pions. Indeed, the proper time for the formation of the produced particles is commonly assumed to be of the order 1 fm/c in the comoving frame. Because the main part of the produced pions is quite relativistic at high incident energies, their formation time should be long enough in the reference frame of calculation to prevent them from interacting with the baryon-rich fluids. However, this argument is qualitative rather than quantitative and hence requires further verification. The first attempt to do this was undertaken by the Frankfurt group [13], which started to explore an opposite extreme. They assumed that the produced pions immediately thermalize, forming a baryon-free fluid (or a "fireball" fluid, in terms of [13]), and interact with the baryon-rich fluids. No formation time was allowed, and the strength of the corresponding interaction was guessed rather than microscopically estimated. This opposite extreme, referred to as a (2 + 1) fluid model and being not quite justified either, yielded results substantially different from those of the free-streaming approximation. This was one of the reasons why in subsequent applications the Frankfurt group neglected the interaction between baryon-free and baryon-rich fluids while keeping the produced pions thermalized [14,15], thus effectively restoring the free-streaming approximation. However, the assumed immediate thermalization of the fireball fluid together with the lack of interaction with baryon-rich fluids still was not a consistent approximation.

In the present article we introduce an extension of the multifluid approach for simulating heavy-ion collisions, i.e., a three-fluid model with formation time. This model is a straightforward extension of the two-fluid model with radiation of direct pions [10–12] and (2 + 1)-fluid model [13–15]. We extend the above models in such a way that the created baryon-free fluid (which we call a "fireball" fluid, according to the Frankfurt group) is treated on equal footing with the baryon-rich ones. This implies that we allow a certain formation time for the fireball fluid, during which the matter of the fluid propagates without interactions. Moreover, we assume that the fireball matter gets quickly thermalized after its formation. The latter approximation is an enforced one, because we deal with the hydrodynamics rather than with kinetics. The interaction between fireball and baryon-rich fluids is estimated based on elementary cross sections. A brief account of this model has been already reported in Ref. [23].

The formation time (τ) is a conventional tool of the hadronic physics, which is associated with a finite time of string formation. It is incorporated in kinetic transport models such as UrQMD [24] and HSD [25]. In dense medium the separate strings can already interact; this is the reason of introduction of junctions and formation of color ropes. In fact, this string interaction is a method of extending the treatment beyond the approximation of binary collisions that is inherent to the conventional Boltzmann equation. This interaction does not invalidate the concept of formation time but rather extends it to the case of multiparticle collisions. The concept of strings becomes irrelevant in the deconfined state of matter. Here there are two points of view: (i) quarks and gluons are instantly produced accordingly to the QCD perturbation theory or (ii) they are mediated by a coherent color field [26,27], i.e., first the coherent color field is produced that subsequently decays into incoherent fluctuations—quarks and gluons. The first mechanism implies that $\tau = 0$, whereas the second one still makes room for a finite τ. Therefore, the fitted value of τ may help to distinguish between these two mechanisms of the QGP production.

The developed code allows calculations with various equations of states (EOS), which enter as a separate block of the code. We have started with the simplest, purely hadronic EOS that involves only a simple density-dependent mean field providing saturation of cold nuclear matter at normal nuclear density $n_0 = 0.15$ fm^{-3} and with the proper binding energy -16 MeV. This EOS is a natural reference point for any other more elaborate EOS. Much to our surprise, this trivial EOS turned out to be able to reasonably reproduce a great body of experimental data. Taking advantage of the modern computers, substantial work has been also done on improvement of numerics of the model. These results are reported in this article.

II. THREE-FLUID HYDRODYNAMIC MODEL WITH DELAYED FORMATION

The derivation of equations of the three-fluid model presented below is in fact only an illustration of physical assumptions that this model is based on. Indeed, the Boltzmann equation, from which this derivation starts, strictly speaking is inapplicable to a dense and strongly interacting matter. Therefore, the applicability of the three-fluid model to heavy-ion collisions is certainly an assumption that should be verified in comparison with experimental data. However, this is a general situation with dense systems even in simpler cases. The basic reason for introduction of the three-fluid approximaion is simulation of the finite stopping power, which is important at the formation stage of the initial hot and dense blob of nuclear matter. In this sense, it is an alternative to constructing this initial blob by means of either various kind kinetic transport models [20] or model assumptions [21,22].

A. Basic formulation

Unlike the conventional hydrodynamics, where local instantaneous stopping of projectile and target matter is assumed, a specific feature of the dynamic three-fluid description is a finite stopping power resulting in a counterstreaming regime of leading baryon-rich matter. Experimental rapidity distributions in nucleus-nucleus collisions support this counterstreaming behavior, which can be observed for incident energies between few and 200*A* GeV. The basic idea of a three-fluid approximation to heavy-ion collisions [10,28] is that at each space-time point $x = (t, \mathbf{x})$ the generally nonequilibrium distribution function of baryon-rich matter, $f_{\rm br}(x, p)$ can be represented as a sum of two distinct contributions

$$f_{\rm br}(x, p) = f_p(x, p) + f_t(x, p), \tag{1}$$

initially associated with constituent nucleons of the projectile (p) and target (t) nuclei. In addition, newly produced particles, populating the midrapidity region, are associated with a fireball (f) fluid described by the distribution function $f_f(x, p)$. Therefore, the three-fluid approximation is a minimal way to simulate the finite stopping power at high incident energies. Note that both the baryon-rich and fireball fluids may consist of any type of hadrons and/or partons (quarks and gluons), rather than only nucleons and pions. However, here and below we suppress the species label at the distribution functions for the sake of transparency of the equations.

With the above-introduced distribution functions f_α ($\alpha = p, t, f$), the coupled set of relativistic Boltzmann equations looks as follows:

$$p_\mu \partial_x^\mu f_p(x,p) = C_p(f_p, f_t) + C_p(f_p, f_f), \tag{2}$$
$$p_\mu \partial_x^\mu f_t(x,p) = C_t(f_p, f_t) + C_t(f_t, f_f), \tag{3}$$
$$p_\mu \partial_x^\mu f_f(x,p) = C_f(f_p, f_t) + C_f(f_p, f_f) + C_f(f_t, f_f), \tag{4}$$

where C_α denote collision terms between the constituents of the three fluids. We have omitted intrafluid collision terms, like $C_p(f_p, f_p)$, because below they will be canceled anyway. The displayed interfluid collision terms have a clear physical meaning: $C_{p/t}(f_p, f_t)$, $C_{p/t}(f_{p/t}, f_f)$, and $C_f(f_{p/t}, f_f)$ give rise to friction between p, t, and f fluids, and the term $C_f(f_p, f_t)$ takes care of particle production in the midrapidity region. Note that up to now we have done no approximation, except for hiding intrafluid collision terms.

Let us proceed to approximations that justify the term *fluids* having been used already. We assume that constituents within each fluid are locally equilibrated, both thermodynamically and chemically, i.e., that f_α are equilibrium distributions. In particular, this implies that the intrafluid collision terms are indeed zero. This assumption relies on the fact that intrafluid collisions are much more efficient than interfluid interactions in driving a system to equilibrium. As applied to the fireball fluid, this assumption requires some additional comments, related to the concept of a finite formation time. During the proper formation time τ after production, the fireball fluid propagates freely, interacting neither with itself nor with the baryon-rich fluids. After this time interval, the fireball matter starts to interact with both itself and the baryon-rich fluids and, as a result, locally thermalizes. Being heated up, these three fluids may contain not only hadronic and but also deconfined quark-gluon species, depending on the EOS used.

The above assumption suggests that interaction between different fluids should be treated dynamically. To obtain the required dynamic equations, we first integrate the kinetic Eqs. (3)–(4) over momentum and sum over particle species with weight of baryon charge. This way we arrive to equations of the baryon charge conservation

$$\partial_\mu J_\alpha^\mu(x) = 0, \tag{5}$$

for $\alpha = p$ and t, where $J_\alpha^\mu = n_\alpha u_\alpha^\mu$ is the baryon current defined in terms of baryon density n_α and hydrodynamic four-velocity u_α^μ normalized as $u_{\alpha\mu} u_\alpha^\mu = 1$. Equation (5) implies that there is no baryon-charge exchange between p and t fluids, as well as that the baryon current of the fireball fluid is identically zero, $J_f^\mu = 0$. Integrating kinetic Eqs. (3)–(4) over momentum with weight of four-momentum p^ν and summing over all particle species, we arrive at equations of the energy-momentum exchange for energy-momentum tensors $T_\alpha^{\mu\nu}$ of the fluids

$$\partial_\mu T_p^{\mu\nu}(x) = -F_p^\nu(x) + F_{\rm fp}^\nu(x), \tag{6}$$

$$\partial_\mu T_t^{\mu\nu}(x) = -F_t^\nu(x) + F_{\rm ft}^\nu(x), \tag{7}$$

$$\partial_\mu T_f^{\mu\nu}(x) = F_p^\nu(x) + F_t^\nu(x) - F_{\rm fp}^\nu(x) - F_{\rm ft}^\nu(x), \tag{8}$$

where the F_α^ν are friction forces originating from interfluid collision terms in the kinetic Eqs. (3)–(4). F_p^ν and F_t^ν in Eqs. (6) and (7) describe energy-momentum loss of baryon-rich fluids because of their mutual friction. A part of this loss $|F_p^\nu - F_t^\nu|$ is transformed into thermal excitation of these fluids, whereas another part $(F_p^\nu + F_t^\nu)$ gives rise to particle production into the fireball fluid [see Eq. (8)]. $F_{\rm fp}^\nu$ and $F_{\rm ft}^\nu$ are associated with friction of the fireball fluid with the p and t fluids, respectively. Note that Eqs. (6)–(8) satisfy the total energy-momentum conservation

$$\partial_\mu \left(T_p^{\mu\nu} + T_t^{\mu\nu} + T_f^{\mu\nu}\right) = 0. \tag{9}$$

As described above, the energy-momentum tensors of the baryon-rich fluids ($\alpha = p$ and t) take the conventional hydrodynamic form

$$T_\alpha^{\mu\nu} = (\varepsilon_\alpha + P_\alpha) u_\alpha^\mu u_\alpha^\nu - g^{\mu\nu} P_\alpha \tag{10}$$

in terms of the proper energy density, ε_α, and pressure, P_α. For the fireball, however, only the energy-momentum tensor of the formed matter is of practical interest for us. Because we treat the fireball matter as a fluid, we have nothing to do but assume that it is formed already thermalized. This assumption implies that its thermalization time is essentially shorter than its formation time. Moreover, this assumption is in the spirit of other assumptions made: we distinguish the main nonequilibrium associated with finite stopping power and consider all the rest of dynamics within local equilibrium. Thus, only the formed (and by assumption thermalized) part of the energy-momentum tensor is described by this hydrodynamic form

$$T_f^{({\rm eq})\mu\nu} = (\varepsilon_f + P_f) u_f^\mu u_f^\nu - g^{\mu\nu} P_f. \tag{11}$$

Its evolution is defined by an Euler equation with a retarded source term

$$\partial_\mu T_f^{(\mathrm{eq})\mu\nu}(x) = -F_{\mathrm{fp}}^\nu(x) - F_{\mathrm{ft}}^\nu(x) + \int d^4x'\delta^4[x - x' - U_F(x')\tau]\big[F_p^\nu(x') + F_t^\nu(x')\big], \qquad (12)$$

where τ is the formation time and

$$U_F^\nu(x') = \frac{u_p^\nu(x') + u_t^\nu(x')}{|u_p(x') + u_t(x')|} \qquad (13)$$

is a free-propagating four-velocity of the produced fireball matter, which is evidently a timelike four-vector. In fact, this is the velocity at the moment of production of the fireball matter. According to Eq. (12), the energy and momentum of this matter appear as a source in the Euler equation only later, i.e., after the time interval $U_F^0\tau$ on the production, and in different space point $\mathbf{x}' - \mathbf{U}_F(x')\tau$, as compared to the production point $\mathbf{x}'$. From the first glance, one can immediately simplify the r.h.s. of Eq. (12) by performing integration with the δ function. However, this integration is not so straightforward, because the expression under the δ function, $x - x' - U_F(x')\tau = 0$, may have more than one solution with respect to x'. The latter would mean that the matter produced in several different space-time points x' is simultaneously formed in the same space-time point x. This is possible because of the nonlinearity of the hydrodynamic equations.

The above discussed free-propagating fireball matter is, of course, a certain approximation for treating free-streaming particles, which this matter consists of. These produced free-streaming particles are characterized by a distribution function, $f(p)$, in the momentum space, which is determined by their production cross sections, e.g., $p^0 d\sigma_{NN\to\pi X}/d^3p$. In particular, this means that particles get formed at different time instants $\tau_{\mathrm{particle}}\gamma_{\mathrm{particle}}$, depending on the particle velocity ($\gamma_{\mathrm{particle}}$ is the γ factor of the particle). This particle formation is governed by a particle formation time τ_{particle} that differs from our τ we use in the hydrodynamic formulation. Our τ has a meaning of the particle formation time τ_{particle} averaged over the distribution $f(p)$:

$$\tau\,\gamma_f = \int \frac{d^3p}{p^0}\tau_{\mathrm{particle}}\,\gamma_{\mathrm{particle}} f(p) \bigg/ \int \frac{d^3p}{p^0} f(p), \qquad (14)$$

where γ_f is the γ factor of the unformed fireball matter. Equation (14) shows that τ is always longer than τ_{particle}. In particular, if the fireball matter consists of pions, which have approximately thermal distribution with temperature $\approx$100 MeV, then $\tau \approx 2\tau_{\mathrm{particle}}$.

The free-streaming particles are not only formed at different time instants but also in different space points because of the same $f(p)$ distribution. Thus, another approximation we have done consists in neglecting this spacial spread. We could take it into account by changing the δ function in the r.h.s. of Eq. (12) to a smooth distribution of formed particles. This would result in spatial smearing of formation of the fireball fluid. However, at the same time it would make the model formulation more complex, because this smooth distribution of formed particles should depend on the initial $f(p)$ distribution and, hence, on the cross sections, like $p^0 d\sigma_{NN\to\pi X}/d^3p$. Moreover, it would be another source of uncertainty, because the $NN \to \pi X$ process is not the only relevant one. Therefore, for the first estimate of effects of the formation time we avoid these complications.

The residual part of $T_f^{\mu\nu}$ (the free-propagating one) is defined as

$$T_f^{(\mathrm{fp})\mu\nu} = T_f^{\mu\nu} - T_f^{(\mathrm{eq})\mu\nu}. \qquad (15)$$

The equation for $T_f^{(\mathrm{fp})\mu\nu}$ can be easily obtained by taking the difference between Eqs. (8) and (12). If all the fireball matter turns out to be formed before freeze-out, then this equation is not needed. Thus, the three-fluid model introduced here contains both the original two-fluid model with pion radiation [10,11] and the (2 + 1) fluid model [13–15] as limiting cases for $\tau \to \infty$ and $\tau = 0$, respectively.

B. Friction between baryon-rich fluids and their unification

The nucleon-nucleon cross sections at high energies are strongly forward-backward peaked. This fact, which originally served as justification for subdividing baryonic matter into target and projectile fluids, was used in Ref. [18] to estimate the friction forces, F_p^ν and F_t^ν, proceeding from only *NN* elastic scattering. Later these friction forces were calculated [29] based on (both elastic and inelastic) experimental inclusive proton-proton cross sections. In the present calculations we use the following form of the projectile-target friction

$$F_\alpha^\nu = \vartheta^2 \rho_p^\xi \rho_t^\xi \big[\big(u_\alpha^\nu - u_{\bar\alpha}^\nu\big)D_P + \big(u_p^\nu + u_t^\nu\big)D_E\big], \qquad (16)$$

$\alpha = p$ or t, $\bar{\mathrm{p}} = t$, and $\bar{t} = p$. Here, ρ_α^ξ denotes a kind of "scalar densities" of the p and t fluids (see details below),

$$D_{P/E} = m_N V_{\mathrm{rel}}^{\mathrm{pt}} \sigma_{P/E}(s_{\mathrm{pt}}), \qquad (17)$$

where m_N is the nucleon mass, $s_{\mathrm{pt}} = m_N^2(u_p^\nu + u_t^\nu)^2$ is the mean invariant energy squared of two colliding nucleons from the p and t fluids,

$$V_{\mathrm{rel}}^{\mathrm{pt}} = \big[s_{\mathrm{pt}}\big(s_{\mathrm{pt}} - 4m_N^2\big)\big]^{1/2}\big/2m_N^2 \qquad (18)$$

is the mean relative velocity of the p and t fluids, and $\sigma_{P/E}(s_{\mathrm{pt}})$ are determined in terms of nucleon-nucleon cross sections integrated with certain weights (see [10,11,29] for details):

$$\sigma_P(s_{\mathrm{pt}}) = \int_{\theta_{\mathrm{c.m.}}<\pi/2} d\sigma_{NN\to NX}\left(1 - \cos\theta_{\mathrm{c.m.}}\frac{p_{\mathrm{out}}}{p_{\mathrm{in}}}\right), \qquad (19)$$

$$\sigma_E(s_{\mathrm{pt}}) = \int_{\theta_{\mathrm{c.m.}}<\pi/2} d\sigma_{NN\to NX}\left(1 - \frac{E_{\mathrm{out}}}{E_{\mathrm{in}}}\right). \qquad (20)$$

Here the integration is restricted to the forward hemisphere ($\theta_{\mathrm{c.m.}} < \pi/2$) of the center-of-mass (c.m.) scattering angles $\theta_{\mathrm{c.m.}}$, $p_{\mathrm{in}} = (s_{\mathrm{pt}}/4 - m_N^2)^{1/2}$ and $E_{\mathrm{in}} = s_{\mathrm{pt}}^{1/2}/2$ are the incoming momentum and energy of the nucleon before the scattering in the *NN* c.m. frame, respectively, and p_{out} and E_{out} are the corresponding out-coming quantities. $\sigma_P(s_{\mathrm{pt}})$ is a kind of a transport cross section, which is nonzero at any physical s_{pt}, as it is seen from Eq. (19). At the same time, the $\sigma_E(s_{\mathrm{pt}})$ quantity, which is responsible for the fireball production, is zero for s_{pt} below the inelastic threshold. In particular, the latter feature makes $D_E = 0$, and hence the friction $F_\alpha = 0$, at vanishing relative velocity $u_p - u_t = 0$. The overall ϑ^2 factor in Eq. (16) is associated with unification of p and t fluid into a single one [see Eq. (23)], when their relative velocity gets small enough.

The above friction (16) is a certain extension of that derived in Ref. [29] and used in Refs. [10–14]. This original derivation was performed under assumption that baryon-rich fluids consist of only nucleons, or baryons, assuming that baryon-baryon cross sections are similar to proton-proton ones. Therefore, in the original expression for F_α^ν [10–14,29] modified scalar densities of the p and t fluids are substituted by corresponding baryon densities (with $\xi_h = \xi_q = 1$ and $\vartheta^2 = 1$, see below). However, this original calculation is incomplete, because it does not take into account (i) various mesonic (and, maybe, quark and gluonic) species produced in the collision, (ii) possible multiparticle interactions that are quite probable in the dense medium, (iii) possible medium modifications of cross sections and effective masses, and (iv) quark and gluon interactions, if the system happens to undergo the phase transition to the quark-gluon phase. Moreover, (v) even experimental cross sections between hadronic species are only poorly known. As for the nonperturbative quark-gluon phase, this is in the range of pure speculation.

In view of theses uncertainties, it is reasonable to make provisions for tuning the above friction. For this purpose we introduced tuning factors $\xi(s_{\rm pt})$ in the scalar densities of the p and t fluids

$$\rho_\alpha^\xi(s_{\rm pt}) = \left(\rho_\alpha^{\rm bar.} + \tfrac{2}{3}\rho_\alpha^{\rm mes.}\right)\xi_h(s_{\rm pt}) + \tfrac{1}{3}\left(\rho_\alpha^q + \rho_\alpha^g\right)\xi_q(s_{\rm pt}), \quad (21)$$

where $\rho_\alpha^{\rm bar.}$, $\rho_\alpha^{\rm mes.}$, ρ_α^q, and ρ_α^g are scalar densities of all baryons, all mesons, quarks, and gluons, respectively, defined in the conventional way, i.e.,

$$\rho_a(x) = m_a \int \frac{d^3p}{p_0} f_a(x, p) \quad (22)$$

for the a species of mass m_a which are $\rho_\alpha[T(x), \mu_B(x)]$ in the thermodynamic limit. These scalar densities (but of course, only nucleon ones) result from the original derivation of Ref. [29]. We just extended the recipe of Ref. [29] to other species. In fact, in the nonrelativistic case the scalar density is identical to the usual particle-number density, because the mass m_a in Eq. (22) is canceled by p_0 in the denominator. Moreover, in the relativistic case the scalar density is a natural result, because it is a Lorentz invariant contrary to the particle-number density, which is the fourth component of a four-vector. However, in the relativistic case we run into trouble with gluons and quarks. If one uses current masses for gluons and quarks, the corresponding scalar densities are either identically zero (for gluons) or negligibly small (for u and d quarks). To overcome this problem we imply that either thermal effective masses or constituent masses, depending on particular model, should be used in the scalar densities, or they should be calculated beyond the quasiparticle approximation (e.g., on the lattice).

Factors like 2/3 and 1/3 in Eq. (21) take into account the assumed scaling of cross sections in accordance with the naive valence-quark counting. Note that the original free cross section in Eq. (16) was estimated for the proton-proton pair. In Eq. (21) different tuning factors are introduced for hadronic and quark-gluon phase: ξ_h and ξ_q, respectively. If the system occurs in pure hadronic phase, ξ_h^2 directly scales the cross sections $\sigma_{P/E}$. If the system happens to be in a mixed phase, like in the crossover phase transition, both ξ_h and ξ_q participate in the cross-section scaling. Note that originally the scalar densities depend only on x, cf. Eq. (21). The introduced s-dependent tuning factors make the tuned scalar densities ρ_α^ξ also s dependent. In general, ξ_h and ξ_q could be also assumed to be temperature dependent, because the $\sigma_{P/E}$ are obtained by averaging over certain thermal distributions. Nevertheless, we avoid doing this to keep the number of "fitting degrees of freedom" as low as possible.

When the baryon-rich fluids become decelerated enough, it is reasonable to unify them into a single fluid. This limit is not automatically present in the model formulation and therefore should be stipulated [106]. For this purpose we introduce an auxiliary function

$$\vartheta = 1 - \exp\left[-\left(V_{\rm rel}^{\rm pt}/\Delta V\right)^4\right], \quad (23)$$

where $V_{\rm rel}^{\rm pt}$ is the mean relative velocity of the p and t fluids of Eq. (18) and ΔV is the characteristic velocity of particles inside the flow (the Fermi velocity of nucleons in cold matter or the thermal velocity of particles in hot matter)

$$[1 - (\Delta V)^2]^{-1/2} - 1 = \max_{p,t}\left\{\frac{\varepsilon_F}{m_N}, \frac{3T}{2m_N}\right\}, \quad (24)$$

where ε_F is the Fermi energy corresponding to the baryon density of the fluid, T is temperature of the fluid, and the maximum value is searched over quantities corresponding to the two overlapped (p and t) fluids. Thus, at $V_{\rm rel}^{\rm pt} \gg \Delta V$, $\vartheta = 1$ and the purely two-fluid regime is realized, whereas at $V_{\rm rel}^{\rm pt} \ll \Delta V$, $\vartheta = 0$ and the one-fluid regime takes place, which implies complete equilibration of the overlapping fluids. During the numeric simulation the two-fluid and one-fluid solutions are mixed in proportion ϑ and $1 - \vartheta$, respectively, thus providing a smooth approach to the one-fluid limit. This interpolation procedure concerns the pressure P_α and hydrodynamic three-velocity $\mathbf{v}_\alpha$, i.e., those quantities that are required for the hydrodynamic transport and are nonadditive:

$$\widetilde{P}_\alpha = \vartheta P_\alpha + (1 - \vartheta)\frac{n_\alpha}{n_{\rm tot}} P_{\rm tot}, \quad (25)$$

$$\widetilde{\mathbf{v}}_\alpha = \vartheta \mathbf{v}_\alpha + (1 - \vartheta)\mathbf{v}_{\rm tot}. \quad (26)$$

Here $\widetilde{P}_\alpha$ and $\widetilde{\mathbf{v}}_\alpha$ are interpolated quantities for the α fluid, and $P_{\rm tot}, \mathbf{v}_{\rm tot}, n_{\rm tot}$, etc., are quantities derived from the total baryon density $J_{\rm tot}^0 = J_p^0 + J_t^0$ and the 0ν components of the total baryon-rich energy-momentum tensor $T_{\rm tot}^{0\nu} = T_p^{0\nu} + T_t^{0\nu}$, assuming that p and t fluids are unified. The difference between P_α and $P_{\rm tot}$, and between $\mathbf{v}_\alpha$ and $\mathbf{v}_{\rm tot}$, respectively, is as follows. From the solution of hydrodynamic Eqs. (5)–(7) and (12) at each time step we obtain hydrodynamic quantities J_α^0, $T_\alpha^{0\nu}$, and $T_f^{({\rm eq})0\nu}$. At the same time, we need, in particular, the pressure and hydrodynamic four-velocity to proceed to the next time step. We have to calculate them based on the above hydrodynamic quantities and the EOS. Here we can proceed in two ways. The conventional way of the multifluid hydrodynamics consists in calculating the pressure and four-velocity for each fluid, i.e., solely based on the J_α^0 and $T_\alpha^{0\nu}$ quantities related to this fluid. This way we arrive at P_α and $\mathbf{v}_\alpha$, which completely preserve the multifluid character of the solution. Alternatively, we can completely abandon the multifluid nature and assume that we deal with a locally equilibrium piece of baryon-rich matter, which is characterized by $J_{\rm tot}^0$ and $T_{\rm tot}^{0\nu}$, and then calculate the pressure and four-velocity of this "unified" piece. Thereby we arrive at $P_{\rm tot}$ and $\mathbf{v}_{\rm tot}$, which describe unified baryon-rich fluids as if they are mutually stopped.

This unification procedure was first proposed by the Los Alamos group [8] and then used in subsequent applications of the multifluid dynamics [11–14]. Evidently, this procedure also affects the stopping power and therefore can be added to the above list of uncertainties associated with the friction force F_α^ν. Other criteria of unification may produce different observable stopping, as it was shown in Ref. [15]. However, we prefer to keep the original criterion, keeping in mind that this is an important part of the stopping prescription.

As compared to the already conventional unification procedure described above, we have also introduced ϑ^2 factor in the friction force itself, cf. Eq. (16). It is justified, because only the ϑ fraction of each baryon-rich fluid remains in the two-fluid regime, as it follows from the above discussion. Therefore, to be consistent with the above unification procedure, we should keep only this ϑ fraction of the density of each fluid, ρ_α^ξ, in the friction term.

As it has been already mentioned, the way, in which the unification procedure is realized, affects the stopping of the nuclear matter. In fact, it is possible to avoid this artificial unification procedure. As it was shown in Refs. [16,28], the formulation of the multifluid dynamics in terms of mean fields rather than of the EOS results in automatic unification of mutually stopped matter. However, the problem of such mean-field formulation is that the mean fields become unrealistically strong at high relative velocities of counterstreaming matter, whereas they should die out because to momentum dependence of self-energies, as it was advocated in the HSD model [25]. Therefore, for the domain of high incident energies the present approach, based on a separate EOS in each fluid and complemented by the unification procedure, is certainly preferable as compared to the pure mean-field formulation of Refs. [16,28]. The latter formulation is definitely advantageous at moderate incident energies of the order of 1A GeV.

Equations (5)–(7) and (11), supplemented by a certain EOS and expressions for friction forces F^ν, form a full set of equations of the relativistic three-fluid hydrodynamic model. The only quantity we still need to define, in terms of hydrodynamic variables and some cross sections, is the friction of the fireball fluid with the p and t fluids, $F_{\rm fp}^\nu$ and $F_{\rm ft}^\nu$.

C. Interaction between fireball and baryon-rich fluids

Our aim here is to estimate the scale of the friction force between the fireball and baryon-rich fluids, similarly to that done before for baryon-rich fluids [29]. To this end, we consider a simplified system, where all baryon-rich fluids consist only of nucleons, as the most abundant component of these fluids, and the fireball fluid contains only pions.

For incident energies from 10A (AGS) to 200A GeV (SPS), the relative nucleon-pion energies are in the resonance range dominated by the Δ resonance. To estimate this relative energy we consider a produced pion, being at rest in the center of mass of the colliding nuclei, $p = \{m_\pi, 0, 0, 0\}_{\rm c.m.}$. Baryon-rich fluids decelerate each other during their interpenetration. This means that the nucleon momentum q should be smaller than the incident momentum, $q_0 = E_N < m_N \gamma_{\rm c.m.}$, where $\gamma_{\rm c.m.}$ is the γ factor of the incident nucleon in the c.m. frame. Calculating the invariant relative energy squared $s = (p+q)^2$ at $E_{\rm lab} = 158A$ GeV, we obtain $s^{1/2} < 1.8$ GeV. This range of s precisely covers the resonance region, 1.1 GeV $< s^{1/2} <$ 1.8 GeV [30]. At $E_{\rm lab} = 10A$ GeV we arrive at $s^{1/2} < 1.3$ GeV, which is also within the resonance region. At even lower incident energies the strength of the fireball fluid becomes so insignificant, as compared with thermal mesons in the p and t fluids, that the way of treatment of its interaction with the baryon-rich fluids does not essentially affect the observables. For the same reason we do not apply any special prescription for the unification of the fireball fluid with the baryon-rich fluids, because this may happen only at relatively low incident energies $E_{\rm lab} <$ 10A GeV.

The resonance-dominated interaction implies that the essential process is absorption of a fireball pion by a p or t fluid nucleon with formation of an R resonance (most probably Δ). This produced R resonance still belongs to the original p or t fluid, since its recoil because of absorption of a light pion is small. Subsequently this R resonance decays into a nucleon and a pion already belonging to the original p or t fluid. Symbolically, this mechanism can be expressed as

$$N^\alpha + \pi^f \rightarrow R^\alpha \rightarrow N^\alpha + \pi^\alpha.$$

As a consequence, only the loss term contributes to the kinetic equation for the fireball fluid.

Proceeding from the above consideration, we write down the collision term between fireball-fluid pions and α-fluid nucleons ($\alpha = p$ or t) as follows:

$$C_f(f_\alpha, f_f) = -\int \frac{d^3q}{q_0} W^{N\pi\rightarrow R}(s) f_f^{(\rm eq)}(p) f_\alpha(q), \quad (27)$$

where $s = (p+q)^2$,

$$W^{N\pi\rightarrow R}(s) = \tfrac{1}{2}\sqrt{\left(s - m_N^2 - m_\pi^2\right)^2 - 4m_N^2 m_\pi^2}\,\sigma_{\rm tot}^{N\pi\rightarrow X}(s)$$

is the rate to produce a baryon R resonance and $\sigma_{\rm tot}^{N\pi\rightarrow X}(s)$ is the parametrization of experimental pion-nucleon cross sections [30]. Here, only the distribution function of formed (and hence thermalized) fireball pions, $f_f^{(\rm eq)}$, enters the collision term, because the nonformed particles do not participate in the interaction by assumption.

Multiplying $C_f(f_\alpha, f_f)$ by the four-momentum p^ν and integrating the result over momentum, we arrive at

$$\begin{aligned} F_{f\alpha}^\nu(x) &= \int \frac{d^3q}{q_0} \frac{d^3p}{p_0} p^\nu W^{N\pi\rightarrow R}(s) f_f^{(\rm eq)}(p) f_\alpha(q) \\ &\simeq \frac{W^{N\pi\rightarrow R}(s_{f\alpha})}{m_\pi u_f^0} \left[\int \frac{d^3q}{q_0} f_\alpha(q)\right] \end{aligned}$$

$$\times \left[\int \frac{d^3p}{p_0} p^0 p^\nu f_f^{(\mathrm{eq})}(p) \right]$$
$$= D_{f\alpha} \frac{T_f^{(\mathrm{eq})0\nu}}{u_f^0} \rho_\alpha, \tag{28}$$

where we substituted p^0 and s by their mean values, $\langle p^0 \rangle = m_\pi u_f^0$ and $s_{f\alpha} = (m_\pi u_f + m_N u_\alpha)^2$, and introduced the transport coefficient

$$D_{f\alpha} = \frac{W^{N\pi \to R}(s_{f\alpha})}{m_N m_\pi} = V_{\mathrm{rel}}^{f\alpha} \sigma_{\mathrm{tot}}^{N\pi \to R}(s_{f\alpha}). \tag{29}$$

Here, $V_{\mathrm{rel}}^{f\alpha} = [(s_{f\alpha} - m_N^2 - m_\pi^2)^2 - 4m_N^2 m_\pi^2]^{1/2}/(2m_N m_\pi)$ denotes the mean invariant relative velocity between the fireball and the α fluids. Thus, we have expressed the friction $F_{f\alpha}^\nu$ in terms of the fireball-fluid energy-momentum density $T_f^{0\nu}$ (of only pions as yet), the scalar density ρ_α of the α fluid (of only nucleons as yet), and a transport coefficient $D_{f\alpha}$. Note that this friction is zero until the fireball pions are formed, because $T_f^{(\mathrm{eq})0\nu} = 0$ during the formation time τ.

In fact, the above treatment is an estimate of the friction terms rather than their strict derivation. All the uncertainties mentioned in the previous subsection are well applied to the case under consideration. This peculiar way of evaluation is motivated by the form of the final result [Eq. (28)]. An advantage of this form is that m_π and any other mass do not appear explicitly, and hence it allows a natural extension to any content of the fluid, including deconfined quarks and gluons, assuming that $D_{f\alpha}$ represents just a scale of the transport coefficient. Performing such extension, we assume that $T_f^{0\nu}$ represents the total energy-momentum density of the fireball fluid and ρ_α is the total scalar density of the α fluid, i.e., $\rho_\alpha \equiv \rho_\alpha^{\xi=1}$ in terms of Eq. (21). Here we have omitted tuning ξ factors in the scalar density ρ_α, because in this case their effect is very similar to that of the formation time, which switches on/off the interaction at various stages and thereby effectively changes its strength.

D. Freeze-out

The hydrodynamic simulation is terminated by a freeze-out procedure. Though this method (as applied to high-energy physics) was first proposed almost 50 years ago [31], this is still an actual problem that is actively discussed. The method was intuitively clear and easily applicable. However, as was shown by Cooper and Frye [32], the Milekhin's method violates the energy conservation. To remedy the situation, they proposed their own recipe. The Cooper-Frye recipe [32] was not free of problems as well. It gives negative contribution to the particle spectrum in some kinematic regions in which the normal vector to the freeze-out hypersurface is spacelike. This negative contribution corresponds to frozen-out particles returning to the hydro phase. Cutoff of this negative contribution again returns us to the violation of the energy conservation. To get rid of this negative spectrum, a modification of the Cooper–Frye recipe was proposed based on a cut-Jüttner distribution [33–36]. In this distribution the part of the Jüttner distribution that gave the negative spectrum is simply cut off. To preserve the particle and energy conservation, the rest of Jüttner distribution is renormalized, effectively resulting in a new temperature and chemical potential (so-called "freeze-out shock"). In fact, this cut-Jüttner recipe has no physical justification, except for practical utility. Moreover, the cut-Jüttner recipe is not supported by schematic kinetic treatment [37] of the transitional region from hydro regime to that of dilute gas and looks like a violence to the nature, making the freeze-out procedure uncontrollable. Recently there was proposed a new freeze-out recipe, a canceling-Jüttner distribution [38], which complies with results of schematic kinetic treatment [37]. However, very recently the authors reported [39] that this canceling-Jüttner distribution is satisfactory only for the spacelike freeze-out, whereas it fails for the timelike one. It should be stressed that this was precisely the schematic kinetic treatment. This region, where the transition from highly collisional dynamics to the collisionless one occurs, is highly difficult for the kinetic treatment and allows hardly any justified simplifications.

All the above considerations of the freeze-out process proceeded from assumption of existing some continuous hypersurface separating the hydro system from the frozen-out gas. Conservation conditions on such hypersurface are constructed in analogy with shock front in hydrodynamics. From the practical point of view, it would mean that we should first run the hydro calculation without any freeze-out and only after that look for a hypersurface where the freeze-out criterion is met. In practice our hydro simulation proceeds in different way. The freeze-out criterion is checked continuously during the simulation. If some parts of the hydro system meet this criterion, they decouple from the hydro calculation. The frozen-out matter escapes from the system, removing all the energy and momentum accumulated in this matter. Therefore, it produces no recoil to the rest of still hydrodynamic system [107]. In particular, it means that the boundary condition on the free surface (between the hydro system and vacuum) is not kept at the same position as in the calculation without freeze-out but moves inside the system. It affects not only the system surface but also the interior. The freeze-out process looks like an evaporation (or fragmentation, on account of final-size grid) first from the system surface and then as a volume fragmentation of the system residue.

In view of the above, we prefer to avoid using not-quite-justified complications of the freeze-out procedure and make use of the simplest (however equally unjustified) original choice of Milekhin [31] with corrected treatment of the energy conservation. The freeze-out criterion we use is

$$\varepsilon_{\mathrm{tot}} < \varepsilon_{\mathrm{frz}}, \tag{30}$$

where

$$\varepsilon_{\mathrm{tot}} = \left(T_p^{00} + T_t^{00} + T_f^{(\mathrm{eq})00}\right)_{\mathrm{proper}} \tag{31}$$

is the energy density of all three fluids in the proper reference frame, where all nondiagonal components of the total energy-momentum tensor are zero,

$$\left(T_p^{\mu\nu} + T_t^{\mu\nu} + T_f^{(\mathrm{eq})\mu\nu}\right)_{\mathrm{proper}}^{\mu\neq\nu} = 0, \tag{32}$$

and $\varepsilon_{\mathrm{frz}}$ is the critical freeze-out energy density. If the freeze-out criterion is met in some space-time point, all three fluids in this point get frozen out and removed from the hydrodynamic evolution. In fact, we freeze-out the fluids in tiny portions, i.e., droplets. This is allowed and even implied by the numerical scheme we use (see Appendix A). Each droplet gets frozen out in its proper reference frame. In terms of the hypersurface, our freeze-out hypersurface is discontinuous and consists of small fragments with normal vectors of local four-velocities. Any transport is prohibited on the nonexistent parts (parallel to the flow velocity) of the surface. In this sense, our freeze-out is more similar to a continuous fragmentation of the system rather than to occurrence of the shock front.

A frozen-out droplet of the α fluid (let it be marked as $i\alpha$) is still characterized by some temperature, baryon, and strange chemical potentials corresponding to a nongas EOS (involving some mean fields) used in the hydro calculation. This is not suitable for calculation of the spectrum of observable particles. First we should release the energy stored in mean fields. To do this, we recalculate temperature ($T^{i\alpha(\text{gas})}$), baryon ($\mu_b^{i\alpha(\text{gas})}$), and strange ($\mu_s^{i\alpha(\text{gas})}$) chemical potentials corresponding to the hadronic gas EOS proceeding from conservations of total energy-momentum, baryon, and strange charges in the droplet. This has been done in the following way. From the solution of hydrodynamic Eqs. (5)–(7) and (12) we know five quantities for each fluid: J_α^0, T_α^{00}, T_α^{01}, T_α^{02}, and T_α^{03}. To interpret them in thermodynamic terms, we should first determine six quantities for each fluid: n_α, ε_α, P_α, and three components of the four-velocity u_α, proceeding from above five hydrodynamic quantities, see Eqs. (10) and (11). Naturally, five equations are not enough for determining six quantities. Therefore, we add one more equation to this set—the EOS. Thus, the resulting thermodynamic quantities turn out to be EOS dependent. In particular, this scheme with the gas EOS results in a change of the hydrodynamic four-velocity ($u^\mu_{i\alpha(\text{gas})}$) as compared to that calculated with the EOS used in the hydrodynamic simulation. The second, already conventional step consists in determination of temperature and chemical potentials proceeding from baryonic, strange and energy densities and pressure.

This is a kind of "freeze-out shock," which, however, is completely different from that induced by the cut-Jüttner recipe. Now in terms of frozen-out droplets of various α fluids, the spectrum of observable hadrons of a species with e_b^a baryon and e_s^a strange charges can be expressed as follows:

$$E\frac{dN_a}{d^3p} = \sum_{i\alpha}\frac{g_a V_{i\alpha}^{(\text{proper})}}{(2\pi)^3} \times \frac{p_\mu u^\mu_{i\alpha(\text{gas})}}{\exp\left[\left(p_\mu u^\mu_{i\alpha(\text{gas})} - e_b^a\mu_b^{i\alpha(\text{gas})} - e_s^a\mu_s^{i\alpha(\text{gas})}\right)/T^{i\alpha(\text{gas})}\right] \pm 1}, \tag{33}$$

where g_a is degeneracy of the a particle, $V_{i\alpha}^{(\text{proper})}$ is the volume of the $i\alpha$ droplet in its rest frame, and the sum runs over all frozen-out droplets of all fluids. If the a species is a baryon, the upper sign (+) should be taken in the denominator, if it is a meson, the lower sign (−).

The described "fragmentation" method of freeze-out precisely conserves energy-momentum and various charges. However, it is also not free from problems. The microscopic justification of this method is still lacking. The problem of returning frozen-out particles into the hydrodynamic phase still persists. Certainly, further search for a reliable freeze-out procedure is needed. A more consistent way of performing the freeze-out, the method of "continuous emission," was proposed in Ref. [40]. Avoiding sharply defined freeze-out hypersurface, this method considers a continuous emission of particles from a finite volume, governed by their mean free paths. Its predictions at the level of observables differ from those based on the Cooper-Frye recipe [41]. Unfortunately, this method is very difficult for the numerical implementation.

III. SIMULATIONS OF NUCLEUS–NUCLEUS COLLISIONS

The 3D code for the 3-fluid model was constructed by means of modifying the existing 2-fluid code of Refs. [10,12]. The numeric scheme of the code is based on the modified particle-in-cell method [42–45], cf. Appendix A. The strategy of our simulations is as follows. At the first step, we try to reproduce the stopping power observed in proton rapidity distributions by means of fine fitting of friction forces of the model. In principle, friction forces are EOS dependent both through scalar densities [Eq. (21)] and because of medium modifications of cross sections. In spite of this, our friction is just schematically estimated proceeding from vacuum proton-proton cross sections and therefore does not comply with the EOS used. This is so even for the simplest hadronic EOS, used in the present article. The list of uncertainties relevant to the friction forces was discussed in Sec. II B. In view of this, the strategy of fine fitting of friction forces is quite reasonable. Note that the success of such fit is not obvious in advance because by means of two functions $\xi_h(s)$ and $\xi_q(s)$ of a single variable [in the present case, only $\xi_h(s)$], see Eq. (21), we fit a function of three variables: rapidity, incident energy, and impact parameter. It is worthwhile to mention that the fit of the friction is EOS dependent. It allows to reproduce proton rapidity distributions only with the particular EOS. In general, another EOS requires different fit.

After the friction forces have been fixed, we tune the freeze-out energy density (in the reasonable range) to reproduce transverse-mass proton spectra and multiplicities of produced pions at comparatively low incident energies $E_{\text{lab}} \lesssim 20A$ GeV. At higher incident energies, the pion multiplicity turns out to be weakly sensitive to variation of the freeze-out energy density. In principle, the freeze-out criterion could be different for different particle species and even for the chemical and thermal freeze-out. However, we keep it unique for all the cases to avoid multiplication of fitting parameters. Therefore, fit of these quantities by means of a single parameter is not an obvious task. At higher incident energies $E_{\text{lab}} \gtrsim 30A$ GeV the pion multiplicities become sensitive to the formation time τ. Therefore, the next step consists in tuning τ (again in the reasonable range) to reproduce them again at higher incident energies. These subsequent steps are simplified by the fact that proton rapidity distributions are only slightly sensitive to variation of τ and the freeze-out energy density. After all these steps, all the model parameters got fixed, and all further calculations give pure predictions of the model. Our final aim is to find a EOS that reproduces in the best way the largest body of the observables of nuclear collisions in the incident energy range $E_{\rm lab} \simeq (1\text{–}160)A$ GeV.

A. Hadronic EOS

We start our simulations with the purely hadronic EOS. This EOS, which was originally used in two-fluid simulations [10–12], was proposed in Ref. [46]. It is a natural reference point for any other more elaborate EOS. The energy density and pressure are constructed as follows:

$$\varepsilon(n_B, T) = \varepsilon_{\rm gas}(n_B, T) + W(n_B), \tag{34}$$

$$P(n_B, T) = P_{\rm gas}(n_B, T) + n_B \frac{dW(n_B)}{dn_B} - W(n_B), \tag{35}$$

where $\varepsilon_{\rm gas}(n_B, T)$ and $P_{\rm gas}(n_B, T)$ are the energy density and pressure of relativistic hadronic gas, respectively, which depend on baryon density n_B and temperature T. The only difference from the ideal gas is that baryons are affected by a mean field $U(n_B)$, i.e., the energy of the a-baryon of mass M_a with momentum $\mathbf{p}$ is $\epsilon_a = (\mathbf{p}^2 + M_a^2)^{1/2} + b_a U(n_B)$, where b_a is the baryon number of the a particle, and the potential $U(n_B)$ is parametrized as follows:

$$U(n_B) = m_N \left[-2b \left(\frac{n_B}{n_0} \right) + c(\gamma + 2) \left(\frac{n_B}{n_0} \right)^{\gamma+1} \right]. \tag{36}$$

It depends only on the density n_B. The self-consistent potential contribution to the energy density, $W(n_B)$, is

$$W(n_B) = \int_0^{n_B} U(n)\, dn. \tag{37}$$

Parameters b, c, and γ are determined from the condition that the cold nuclear matter saturates at $n_0 = 0.15$ fm^{-3} and $\varepsilon(n_0, T = 0)/n_0 - m_N = -16$ MeV, and incompressibility of this nuclear matter is $K = 210$ MeV. Parametrization Eq. (36) results in superluminal sound velocity at densities $n_B/n_0 > 8$. To preserve causality at high n_B, the following form of the energy density

$$\varepsilon(n_B, T{=}0) = n_0 m_N \left[A \left(\frac{n_B}{n_0} \right)^2 + C + B \left(\frac{n_0}{n_B} \right) \right] \tag{38}$$

is used at $n_B/n_0 > 6$. Parameters A, B, and C are determined on the condition that $\varepsilon(n_B, T = 0)$ and its two first derivatives are continuous at $n_B/n_0 = 6$. As seen from Fig. 1, the pressure of this hadronic EOS is within the constraint given by Danielewicz *et al.* extracted from the analysis of flow of nuclear matter [47] at the AGS incident energies.

B. Summary of parameters: Friction, freeze-out, etc.

For the sake of complete account, in this section we summarize the parameters used in the present simulations. The specific reasons for choosing these parameters will be discussed in subsequent sections.

(i) The key quantity is the EOS, which was taken in the simple form of purely hadronic EOS, see Sec.III A. In this EOS, 48 different hadronic species are taken into account. Each hadronic species includes all the relevant isospin states, e.g., the nucleon species includes proton and neutron.

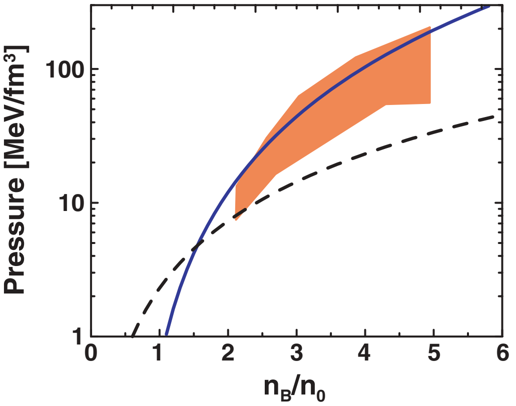

FIG. 1. (Color online) Baryon-density dependence of the pressure at $T = 0$. Shaded region is the constraint [47] derived from experimental data. Solid and dashed lines present the pressure $P(n_B, T = 0)$ and that for the ideal hadronic gas, $P_{\rm gas}(n_B, T = 0)$ [cf. Eq. (35)], respectively.

(ii) The friction between baryon-rich fluids was fitted to reproduce the stopping power observed in proton rapidity distributions, see Sec. III C. For this purpose the original friction, parametrized through experimental inclusive proton-proton cross sections [29], was enhanced by means of the tuning factor ξ_h

$$\xi_h^2(s) = \gamma_h + 2\beta_h [\ln(s/(2m_N)^2)^{1/2}]^{1/4} \tag{39}$$

with $\gamma_h = 1$ and $\beta_h = 0.75$, see Fig. 2. The ξ_q factor is not applicable here because of the pure hadronic nature of the EOS.

(iii) The parameter of freeze-out energy density was fitted to reproduce transverse-mass proton spectra, see Sec. III D, and multiplicities of produced pions at comparatively low incident energies $E_{\rm lab} \lesssim 20A$ GeV, see Sec. III E. It has been taken $\varepsilon_{\rm frz} \simeq 0.2$ GeV/fm^3 at all incident energies with the only exception: $\varepsilon_{\rm frz} \simeq 0.1$ GeV/fm^3

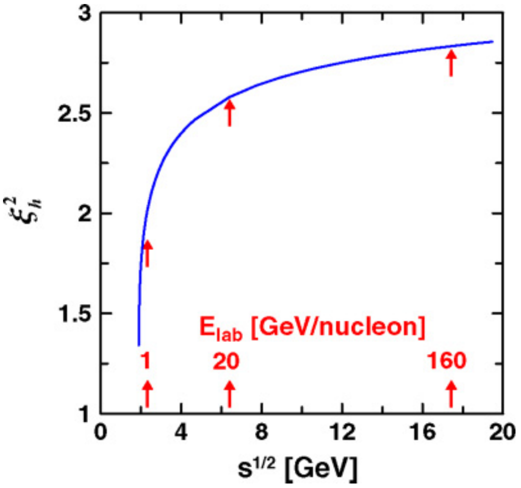

FIG. 2. (Color online) Fitted friction enhancement for the purely hadronic EOS [46] used in simulations, see Eq. (21).

at $E_{\text{lab}} \leqslant s$ $2A$ GeV. These ε_{frz} values are presented as approximate quantities because of the numerical realization of the freeze-out procedure (cf. Appendix A).

(iv) The formation time of the fireball fluid was also fitted to reproduce the pion yield at higher incident energies $E_{\text{lab}} \gtrsim 30A$ GeV, see Sec. III E. It has been taken $\tau = 2$ fm/c. Note that τ is the formation time of a fluid element, consisting of a number of particles, which are generally not thermalized. This implies that the formation time of a separate particle is certainly shorter than τ.

(v) The contributions of strong decays of hadronic resonances (R) into spectra of stable hadrons is taken into account, as it is described in Appendix B. In the present calculation all spectral functions were taken without width

$$A_R(s) = \delta\left(s - m_R^2\right), \tag{40}$$

where m_R is the mass of the R resonance.

(vi) For the reproduction of stable hadron multiplicities it is also important to take into account contributions of weak decays with small values of $c\tau_w$, where τ_w is the inverse width of the decay. Feed back from weak decays of hadrons with $c\tau_w <$ few c.m., i.e., K^0_{short}, Λ, Σ, $\bar{\Lambda}$, and $\bar{\Sigma}$ [108] have been taken into account in yields of stable particles. In particular, this is important for reproduction of the pion multiplicities (Secs. III E and III H and the proper normalization of proton spectra (Secs. III C and III D). However, weakly decaying hadrons with $c\tau_w$ of the order of few meters, i.e., K^0_{long}, K^+ and K^-, were treated as stable particles.

(vii) Light fragment formation (deutrons, tritons, ^{3}He, and ^{4}He) is taken into account in terms of the coalescence model, which is similar to that in Appendix E of Ref. [16]. In Ref. [16], the coalescence coefficients were fitted at the incident energy $0.8A$ GeV. To accommodate this formulation to different incident energies, we change only overall scale of the coalescence (the coefficient C_{coal}), which either enhances ($C_{\text{coal}} > 1$) or reduces ($C_{\text{coal}} < 1$) its strength, keeping ratios of yields of various fragments the same as in Ref. [16], see Table I. At $E_{\text{lab}} > 9A$ GeV we do not apply any coalescence to calculations of nucleon observables, because the respective correction is negligible.

To compare with available experimental data, impact parameters used in calculations were taken either from experimental works, if they were evaluated there, or estimated based on the experimentally declared percentage of the total reaction cross section, corresponding to a particular event selection.

TABLE I. Coalescence parameters C_{coal} used for simulations of Au+Au and Pb+Pb collisions at various incident energies E_{lab}.

E_{lab}, A GeV	1	2	4	6	8	>9
C_{coal}	1.5	1.2	0.8	0.4	0.1	0

C. Proton rapidity distributions: Observable stopping power

The nucleon rapidity distribution basically reflects the stopping power achieved in a nuclear collision. It is defined as

$$\frac{dN_N}{dy} = \int d^2 p_T \left(E\frac{dN_N}{d^3p} + \sum_R E\frac{d^3 N_N^{(R\to N+X)}}{d^3p} \right) \tag{41}$$

in terms of frozen-out spectra of nucleons EdN_N/d^3p, see Eq. (33), and baryonic resonances. The second term under the integral takes into account the contribution of these resonance decays, cf. Eq. (B5), Appendix B, the sum runs over all baryonic resonances R. Integration runs over the transverse (with respect to the beam) momentum p_T.

Either identified protons or difference between positive and negative hadrons are experimentally measured. The latter is associated with the proton-antiproton difference, $(p - \bar{p})$. Because particles are not isotopically distinguished in our model, we estimate the proton distribution simply as

$$\frac{dN_p}{dy} = \frac{Z}{A}\frac{dN_N}{dy}, \tag{42}$$

where Z and A are the proton and mass numbers, respectively, in the colliding (identical) nuclei. This estimate is quite reasonable at comparatively low incident energies. At higher energies, when abundant particle production starts, this recipe somewhat underestimates the proton number. The reason is that newly produced particles tend to restore the isotopic symmetry in the system and hence increase the number of protons as compared with its initial value. The $(p - \bar{p})$ quantity is much less sensitive to the effect of newly produced particles, because their contribution is essentially canceled in the difference $(p - \bar{p})$. Therefore, the Z/A scaling of the nucleon-antinucleon difference is a reasonable approximation for the $(p - \bar{p})$ quantity even at high incident energies. As mentioned above, our aim is to reproduce these distributions in a wide range of incident energies from $1A$ to about $160A$ GeV.

In general, nucleon observables are more robust to variations of physical parameters than other probes, because they are essentially confined by the baryon number conservation. Our first observation is that the nucleon and, in particular, proton rapidity distributions are only weakly sensitive to variation of the freeze-out energy density ε_{frz} and the formation time of the fireball fluid τ. As for ε_{frz}, there is a certain compensation between effects of collective motion and internal excitation. Both these effects produce similar consequences in nucleon spectra. For instance, if we allow the system to evolve longer (the lower ε_{frz}), the collective motion of the matter becomes more developed while its internal excitation drops down (i.e., the matter cools down). This counteraction results only in slight changes in nucleon rapidity distributions. As for the formation time, the density of the produced fireball fluid is not high enough even at the highest considered energy. Therefore, its interaction with baryon-rich fluids only slightly affects the baryon subsystem [23]. This weak dependence on ε_{frz} and τ allows us to use nucleon rapidity distributions to fit the observable stopping power, to which nucleon observables are indeed sensitive.

The second main conclusion is that the original friction between baryon-rich fluids, estimated in Ref. [29] proceeding from free proton-proton cross sections, is evidently insufficient to reproduce observable stopping of nuclear matter. Therefore, this friction is fitted to reproduce this stopping power observed in proton rapidity distributions. For this purpose the original friction was enhanced by means of the tuning factor ξ_h, cf. Eq. (39). Thus, the friction enhancement is the larger, the higher incident energy is. At the lowest considered energy of 1A GeV, the friction turns out to be approximately 2 times enhanced. This is similar to earlier results of the two-fluid model with mean mesonic fields [16]. There it was found out that for the proper reproduction of data on heavy-ion collisions in the energy range from 0.4 to 0.8A GeV the enhancement factor of 3 was required.

Figure 3 illustrates the overall quality of reproduction of experimental data by our hydrodynamic calculations as well as by other transport simulations for two basic incident energies of 10A and 160A GeV. The three-fluid simulations were performed at impact parameters that correspond to the experimentally declared fraction of the total reaction cross section, accumulated in the experimentally selected central events, assuming sharp cutoff in impact parameters. The side bumps of the HSD calculations correspond to spectator parts of colliding nuclei. In our model, these spectator parts were cut off, based on simple criterion: the energy per baryon is less than the nucleon mass, which is the case when a nucleon is at least loosely bound in the matter. As seen, experimental data from different experiments somewhat differ, and therefore one should not expect their reproduction in the model calculations within better than ∼10%. Uncertainties in the impact parameter at the level of about 0.5 fm do not noticeably affect hydrodynamic rapidity spectra. In general, there is a reasonable agreement between hydrodynamic and kinetic calculations.

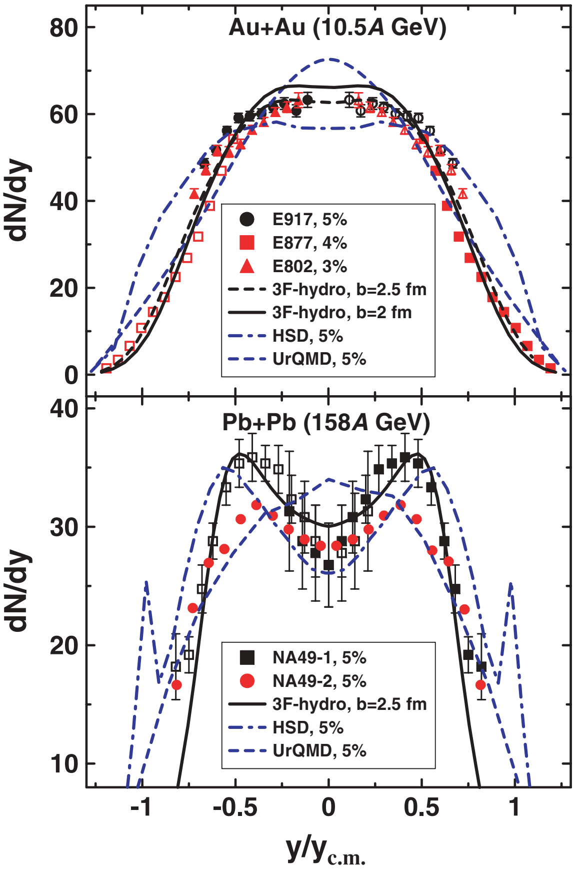

FIG. 3. (Color online) Rapidity spectra of protons (upper panel) and $(p - \bar{p})$ (lower panel) from central heavy-ion collisions. Bold solid lines and bold dashed line (upper panel) correspond to three-fluid hydrodynamic calculations at different impact parameters. Thin dashed-dotted and short-dashed lines are the appropriate UrQMD and HSD model results [48], respectively. Full symbols display measured experimental points, whereas the open ones are those reflected with respect to the midrapidity point. Experimental data are taken by Collaborations E802 [49], E877 [50], E917 [51], and NA49 [52–54]. The percentage shows the fraction of the total reaction cross section, corresponding to experimental selection of central events.

Comparison with experimental data for identified protons is presented in Fig. 4 for the SIS-AGS energy range, where various selections of noncentral nuclear collisions are also considered. Here and below, impact parameters for each set of noncentral interactions were chosen accordingly the experimentally declared fractions of the total reaction cross section, accumulated in the set of experimentally selected events, assuming sharp cutoff in impact parameters.

At the beam energies $E_{\rm lab}$ of the order of 1A GeV, a large fraction of nucleons is produced with low relative velocities. Therefore, they may coalesce forming light fragments. The coalescence formulation accepted here is similar to that in Appendix E of Ref. [16]. Only light fragments (deutrons, tritons, ^{3}He, and ^{4}He) are taken into account. To fit this formulation to different incident energies, we change only overall scale of the coalescence (the coefficient $C_{\rm coal}$) that either enhances ($C_{\rm coal} > 1$) or reduces ($C_{\rm coal} < 1$) its strength, keeping ratios of yields of various fragments the same as in Ref. [16], see Table I.

At the SIS energy we describe reasonably well both proton and deuteron rapidity spectra. The fact that the experimental distribution is somewhat wider than the calculated one can be explained by that the set of experimentally selected events in fact contains a certain admixture of semicentral and peripheral events, whereas the calculation was performed for the single central impact parameter. Indeed, at comparatively low energies the reliable selection of central events is problematic [16]. This noncentral admixture makes the distributions wider as compared to what it would be for the perfect central selection. At this energy the stopping power is rather high. This is seen from both the Gaussian-like shape of the rapidity distributions and also from the fact that the three-fluid results are quite close to those of the conventional one-fluid calculations (see Fig. 4. A separate code was used for these one-fluid calculations. With the increase of the incident energy, the spectrum shape starts to differ from the Gaussian one, getting more and more flat at the midrapidity. The three-fluid model reasonably reproduces the dependence of the spectra on both the incident energy $E_{\rm lab}$ and the impact parameter b. Note that no extra tuning of normalization of the spectra was done. The values of impact parameters were taken from the experimental estimate of centrality of nuclear interactions [51]. Though there are some

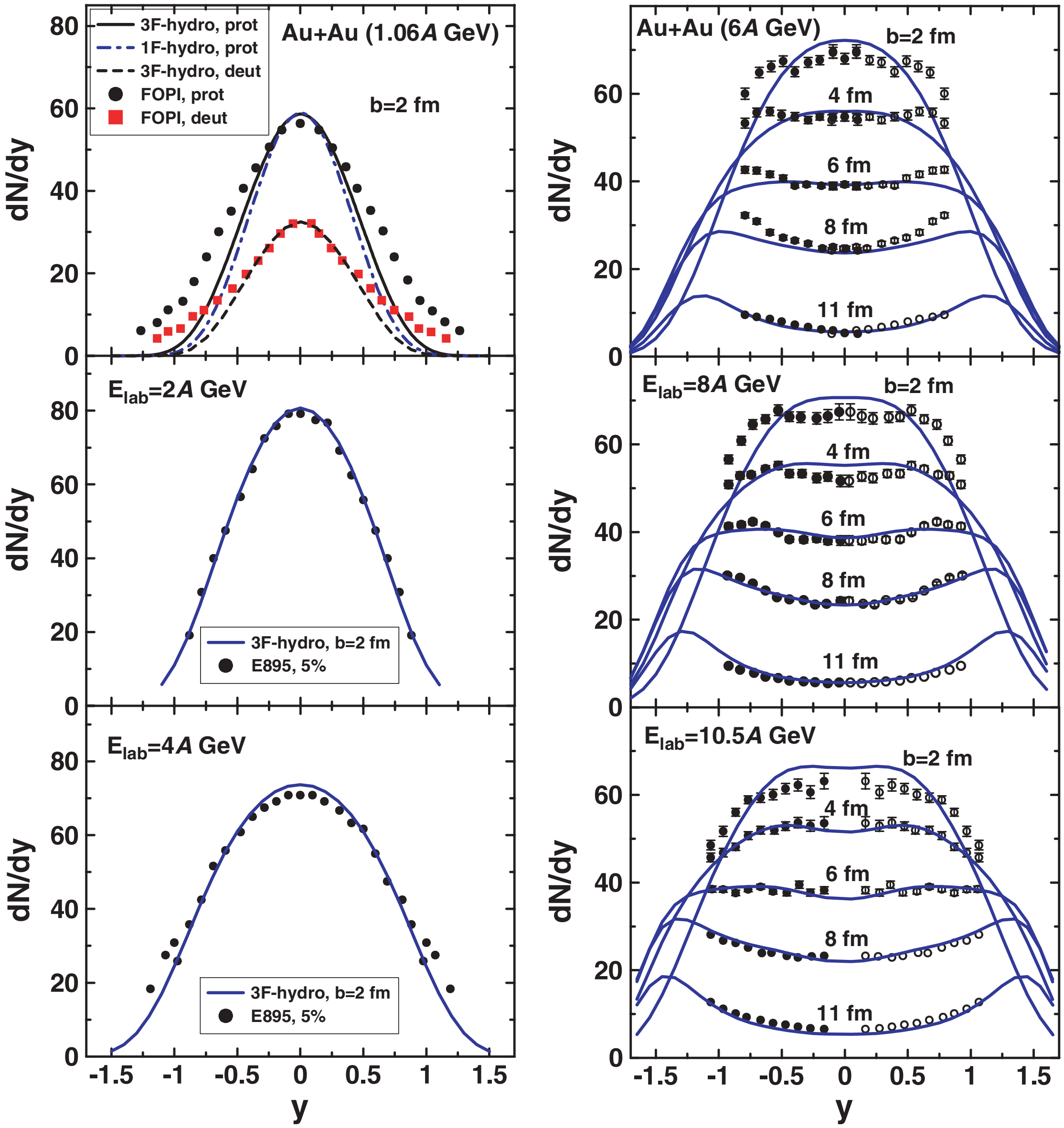

FIG. 4. (Color online) Proton rapidity spectra at SIS and AGS energies for various impact parameters. Solid lines correspond to three-fluid calculations. The dashed line is that for deuteron production. For comparison the one-fluid result is shown by the dotted-dashed line at $E_{\rm lab} = 1.06A$ GeV. Experimental points at different energies are taken from [55] at $E_{\rm lab} = 1.06A$ GeV, [56] at 2A and 4A GeV, and [51] at 6A, 8A, and 10.5A GeV. The percentage indicates the fraction of the total reaction cross section, corresponding to experimentally selected events.

uncertainties in this estimate, we applied no special tuning to values of these impact parameters.

The $(p - \bar{p})$ rapidity spectra at the SPS energies are shown in Fig. 5. A minimum of hydrodynamic distributions dN/dy in the midrapidity region complies with experimental observations at $E_{\rm lab} = 158A$ GeV. It survives at lower incident energies, up to $E_{\rm lab} = 40A$ GeV. This is in contrast to simulations based on kinetic transport codes [48], which predict flat or even peacked distributions in the midrapidity region at $E_{\rm lab} = 40A$ and 80A GeV. Available experimental points here do not allow us to verify these different predictions. Note that experimental points at $E_{\rm lab} = 40A$ and 80A GeV correspond to identified protons, whereas all presented calculations are related to $(p - \bar{p})$.

D. Proton transverse mass distributions

Once the friction has been already fitted to reproduce proton rapidity distributions, we can vary only the freeze-out energy density $\varepsilon_{\rm frz}$ and the formation time of the fireball fluid τ. In contrast to rapidity distributions, the proton transverse-mass distributions turn out to be more sensitive to $\varepsilon_{\rm frz}$, because their slopes reflect the effective temperature of the frozen-out distributions. This is because the internal excitation certainly dominates in the transverse direction as compared to the collective motion. At the same time, these distributions are rather insensitive to τ, as well as all other baryonic (however, not antibaryonic) quantities. Therefore, to reproduce them, we choose $\varepsilon_{\rm frz} \simeq 0.2$ GeV/fm^3 at all incident energies with the only exception: $\varepsilon_{\rm frz} \simeq 0.1$ GeV/fm^3 at $E_{\rm lab} \leqslant 2A$ GeV. As for

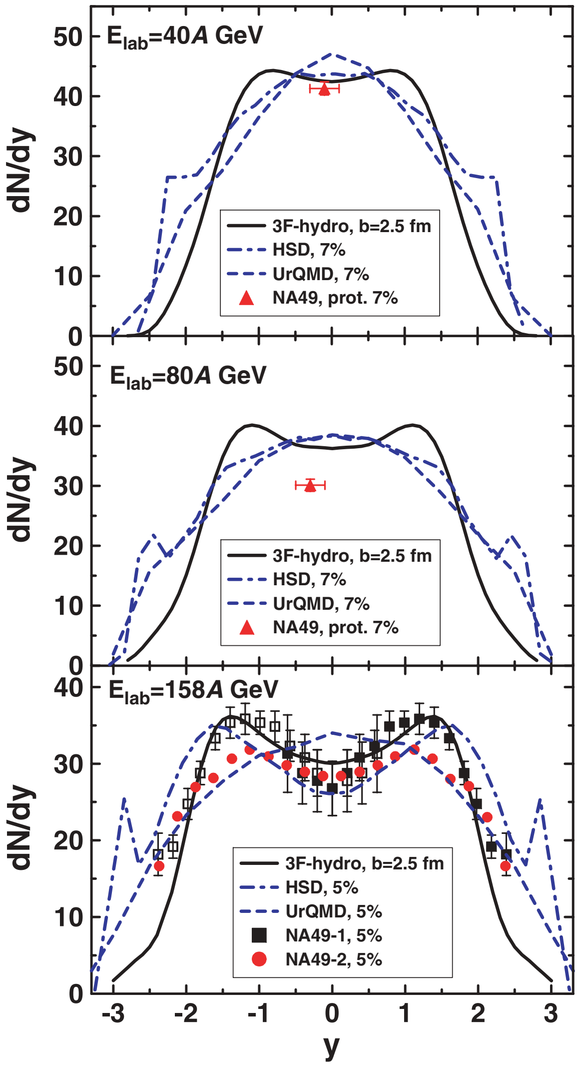

FIG. 5. (Color online) $(p-\bar{p})$ rapidity distribution from central Pb+Pb collisions at SPS energies. Solid lines are three-fluid calculations, whereas dashed-dotted and dashed lines are the corresponding predictions of the HSD and UrQMD models [48], respectively. NA49 experimental data are from Ref. [54] for $E_{\rm lab}=40A$ and $80A$ GeV and from Refs. [52–54] for $E_{\rm lab}=158A$ GeV. The percentage indicates the fraction of the total reaction cross section, corresponding to experimentally selected events.

low energies, $E_{\rm lab}\leqslant 2A$ GeV, we had to reduce $\varepsilon_{\rm frz}$, because otherwise the freeze-out would occur at the very early stage of the collision. The approximate nature of the $\varepsilon_{\rm frz}$ values results from the numerical realization of the freeze-out procedure (cf. Appendix A).

Proton transverse-mass spectra at the AGS energies are exemplified in Fig. 6. They exhibit a typical exponential falloff. As seen, the three-fluid model well reproduces both the normalization and the slopes of this falloff, as well as their rapidity dependence. The right panel of Fig. 6 shows the dependence of the transverse mass distributions at the midrapidity on the impact parameter b. As before, the values of impact parameters were taken from the experimental estimate of centrality of nuclear interaction [51]. The impact-parameter dependence is reasonably reproduced by the model as well even at relatively large impact parameters.

The beam-energy dependence of the proton transverse-mass distributions is presented in Fig. 7 for central Pb+Pb collisions at the SPS energies. Overall, these distributions are in agreement with experimental data. However, the three-fluid model does not exhibit deviation from the exponential falloff at $(m_T-m)\lesssim 0.2$ GeV, observed in experiment, most clearly at $E_{\rm lab}=158A$ GeV. The same feature of the hydrodynamic calculation was earlier reported in Ref. [22]. As it was shown [22], a post-hydro kinetic evolution is required to produce the observable two-slope structure of the m_T spectra. In our model such a post-hydro evolution is absent. It is worthwhile to note that the above problem is not an inalienable feature of any hydrodynamic calculation. For instance, the deviation from the exponential fall-off was reproduced in calculations by Kolb *et al.* [21].

E. Pion rapidity distributions

Production of new particles is closely related to the amount of entropy accumulated in the system. At the late stage of the collision, the system expansion is isoentropic, i.e., the total entropy is conserved. This is indeed so in our simulations, as we have checked it. This fact implies that at high incident energies $E_{\rm lab}\gtrsim 40A$ GeV the total number of produced pions is approximately conserved during this expansion stage, because thermal pions are the dominant component among the produced particles. From the practical point of view, it means that the pion number is approximately independent of the freeze-out energy density $\varepsilon_{\rm frz}$. This is indeed observed in actual simulations. However, at high incident energies the pion number depends on the formation time of fireball fluid τ, because 20÷30% of the pions are produced in the fireball fluid. The shorter τ is, the earlier the fireball fluid starts to interact with baryonic subsystem, and hence the fewer pions survive in this fluid. This implies that the formation time effectively tunes the strength of the fireball-projectile (target) friction, which was only roughly estimated (cf. Sec. II C).

At the first glance, the above speculation contradicts to the pion absorption mechanism (cf. in Sec. II C), which assumes that pions are simply captured by the baryon-rich fluids without loosing their number. However, the pion number is not a conserved quantity. In the baryon-rich fluids the energy of the captured pions is thermally redistributed (accordingly to thermal chemical equilibrium) between kinetic energy of (mainly) baryons and thermally produced (mainly) pions. Therefore, their number is effectively reduced, because in the baryon-free fireball fluid the same energy was mainly accumulated in thermal pions.

At lower incident energies $E_{\rm lab}\lesssim 20A$ GeV, the thermal pion production is not already so dominant but pions are rather produced through decays of resonances. Therefore, their number starts to depend on $\varepsilon_{\rm frz}$. The later freeze-out occurs, the fewer pions are produced. At the same time, the contribution of the produced fireball fluid becomes less important, and hence the τ dependence of the pion multiplicity becomes weak. At intermediate energies $20\lesssim E_{\rm lab}\lesssim 40A$ GeV, there is a moderate dependence of the pion multiplicity on both $\varepsilon_{\rm frz}$

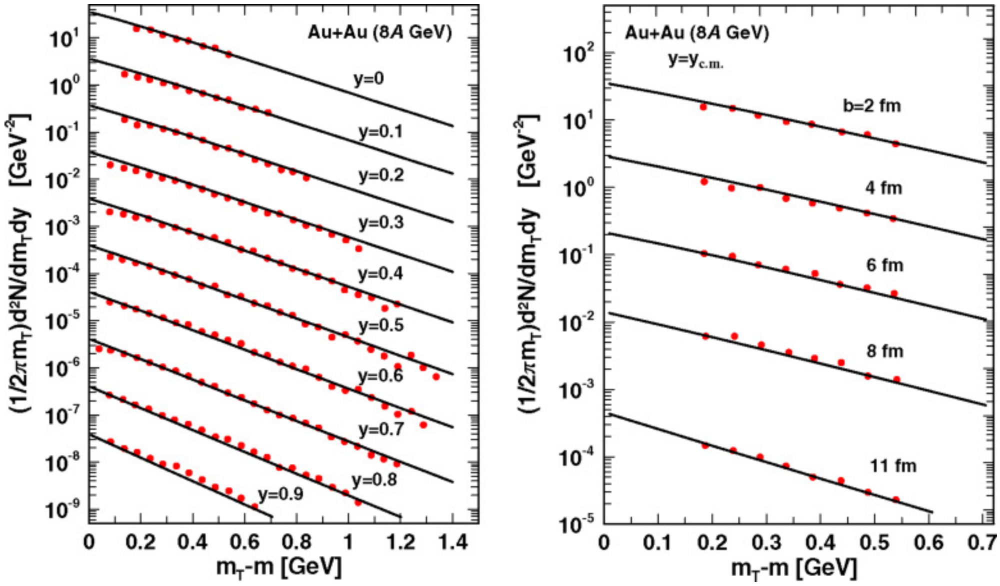

FIG. 6. (Color online) Transverse mass distributions of protons from Au(8*A* GeV)+Au collisions at $b = 2$ fm and different rapidities in the c.m. system (left panel) and at the midrapidity and different impact parameters (right panel), cf. the right panel of Fig. 4. For clarity of representation, every next data set and the corresponding curve (from top to bottom) is multiplied by the additional factor 0.1. Experimental data are from Ref. [51].

and τ. Note that these parameters, $\varepsilon_{\rm frz}$ and τ, mostly affect the overall normalization of pion rapidity spectra, whereas the shape of these spectra mainly depend on the stopping power, which is kept fixed here.

As both the friction and $\varepsilon_{\rm frz}$ have been already fixed above, the pion rapidity distributions at low incident energies $E_{\rm lab} \lesssim 20A$ GeV can be considered as predictions of the model. To reproduce the pion yield at high incident energies $E_{\rm lab} \lesssim 30A$ GeV, the formation time of the fireball fluid has been taken $\tau = 2$ fm/c. Note that τ is the formation time of a fluid element, consisting of a number of particles [cf. Eq. (14) and discussion above it]. This implies that the formation time of a separate particle (pion) at rest is certainly shorter than τ. Assuming that the temperature scale of the fireball fluid is approximately

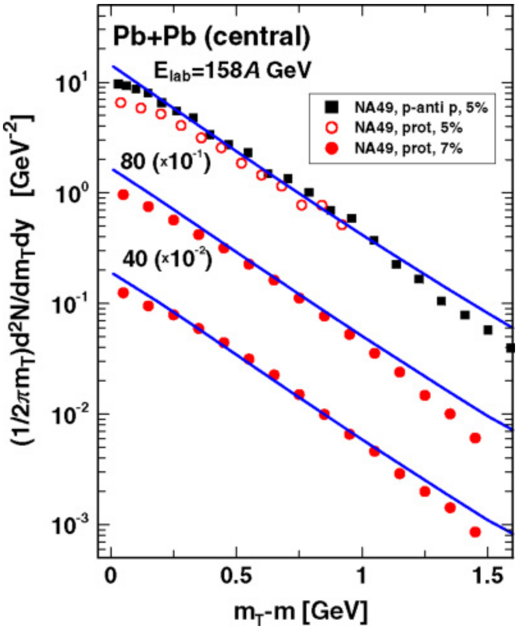

FIG. 7. (Color online) Transverse mass distributions of protons at the midrapidity from central Pb+Pb collisions at incident energies $E_{\rm lab} = 158A$, $80A$, and $40A$ GeV and impact parameter $b = 2.5$ fm, cf. Fig. 5. NA49 experimental data are taken from [52] (squares), [57] (open circles), and [57] (full circles).

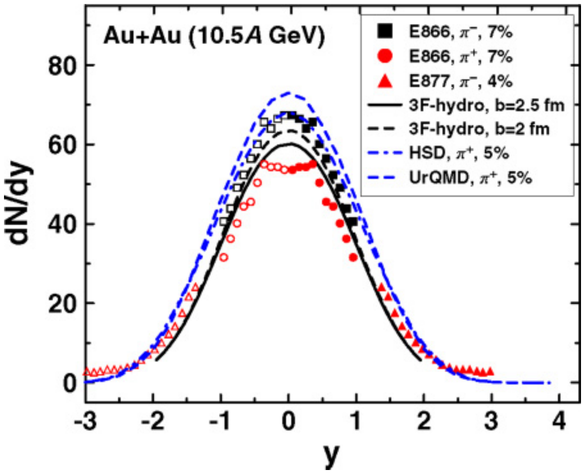

FIG. 8. (Color online) Pion rapidity spectra from central Au(10.5*A* GeV)+Au collisions. Bold solid and dashed lines represent three-fluid calculations at $b = 2.5$ and 2.0 fm, respectively. Thin dashed-dotted and short-dashed lines correspond π^+ spectra from kinetic simulations within HSD and UrQMD models [48]. The π^- (full squares and triangles) and π^+ (full circles) data are measured by E895 [56] and E877 [50] Collaborations. The percentage indicates the fraction of the total reaction cross section, corresponding to experimentally selected events. Open symbols are obtained by reflecting the full ones with respect to the midrapidity.

100 MeV, we estimate that the formation time of a separate pion at rest approximately equals 1 fm/c. This is in good agreement with the estimate of the string-formation time. However, one should keep in mind that the latter value refers to a separate string in vacuum, i.e., without any effects of string interactions (junctions and color-rope formation). At the same time, our τ has an in-medium sense with all these multiparticle effects included. Therefore, their coincidence should be taken with caution. Note that with $\tau = 0$ the multiplicity of pions (as well as other newly produced particles) would be 10%–15% underestimated at high incident energies (>30A GeV). All other observables would remain approximately the same.

Because particles are not isotopically distinguished in our model, we assume that numbers of pions of each charge are equal, i.e., $N_{\pi^+} = N_{\pi^-} = N_{\pi^0} = N_\pi/3$, where N_π is the calculated total number of pions. Of course, this is a rough estimate of π^+ and π^- yields, because N_{π^-} always exceeds N_{π^+} because of the initial isotopic asymmetry of colliding nuclei. Therefore, only if our calculation of $N_\pi/3$ complies with experimental $(N_{\pi^+} + N_{\pi^-})/2$, we refer to this as "a good agreement."

Figure 8 represents pion rapidity distributions in central Au+Au collisions at the incident energy $E_{\rm lab} = 10.5A$ GeV. Sensitivity of this distribution to the variation of the impact parameter is also demonstrated. As seen, the hydrodynamic results indeed fall in between the π^+ and π^- data, hence they comply with these data. In contrast, the π^+ rapidity spectra, calculated in two transport models, HSD and UrQMD models [48] also displayed in Fig. 8, closely follow experimental points but for negative pions. The overestimate of the pion yield by the kinetic models can be attributed to a lack of collective interaction in the EOSs corresponding to those models.

All above said is in fact true for the whole energy range under consideration, as it is demonstrated in Fig. 9.

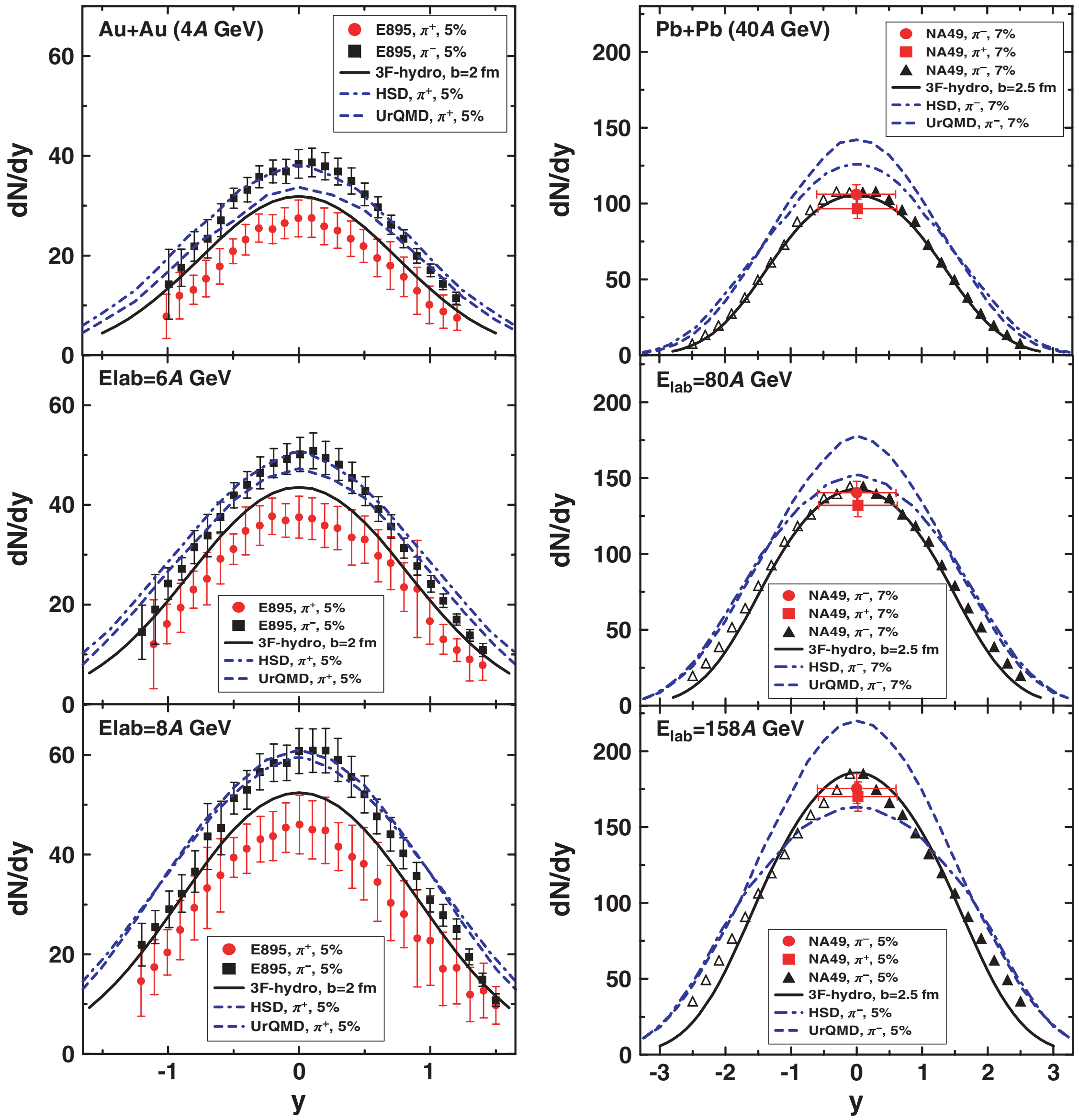

FIG. 9. (Color online) Pion rapidity spectra from central collisions at the AGS (left panel) and SPS (right panel) energies. Experimental points are taken from [56] (AGS energies) and [58] (SPS energies). Notation is the same as in Fig. 8.

The three-fluid model reasonably reproduces the pion distributions, whereas the HSD and UrQMD models certainly overestimate them.

F. Rare particle production

Now all the parameters of the model are fixed. Therefore, all further calculations can be treated as predictions of the three-fluid model.

As an example of the hydrodynamic description of rare channels, the rapidity spectra of Λ and $\bar{\Lambda}$ hyperons are presented in Fig. 10. Contributions from decays of higher resonances are taken into account. Both shape and absolute value of hyperon and antihyperon spectra are reproduced surprisingly well. The Λ hyperons originate mainly from baryon-rich fluids and shapes of their spectra closely follow those of the protons. Although the experimental data are preliminary, one may note that agreement with experiment becomes certainly worse at the incident energy $E_{\text{lab}} = 40A$ GeV. Unfortunately, the only measured point in proton rapidity distribution (see Fig. 5) does not allow us to conclude on either similarity or difference of the Λ and p distributions at this energy. In contrast, $\bar{\Lambda}$ antihyperons are dominantly created in the baryon-free fireball and have typical single-bump thermal spectra.

At the same time the experimental data on antiproton production [60] are certainly overestimated in the our model, as illustrated in Fig. 11. Because particles are not isotopically

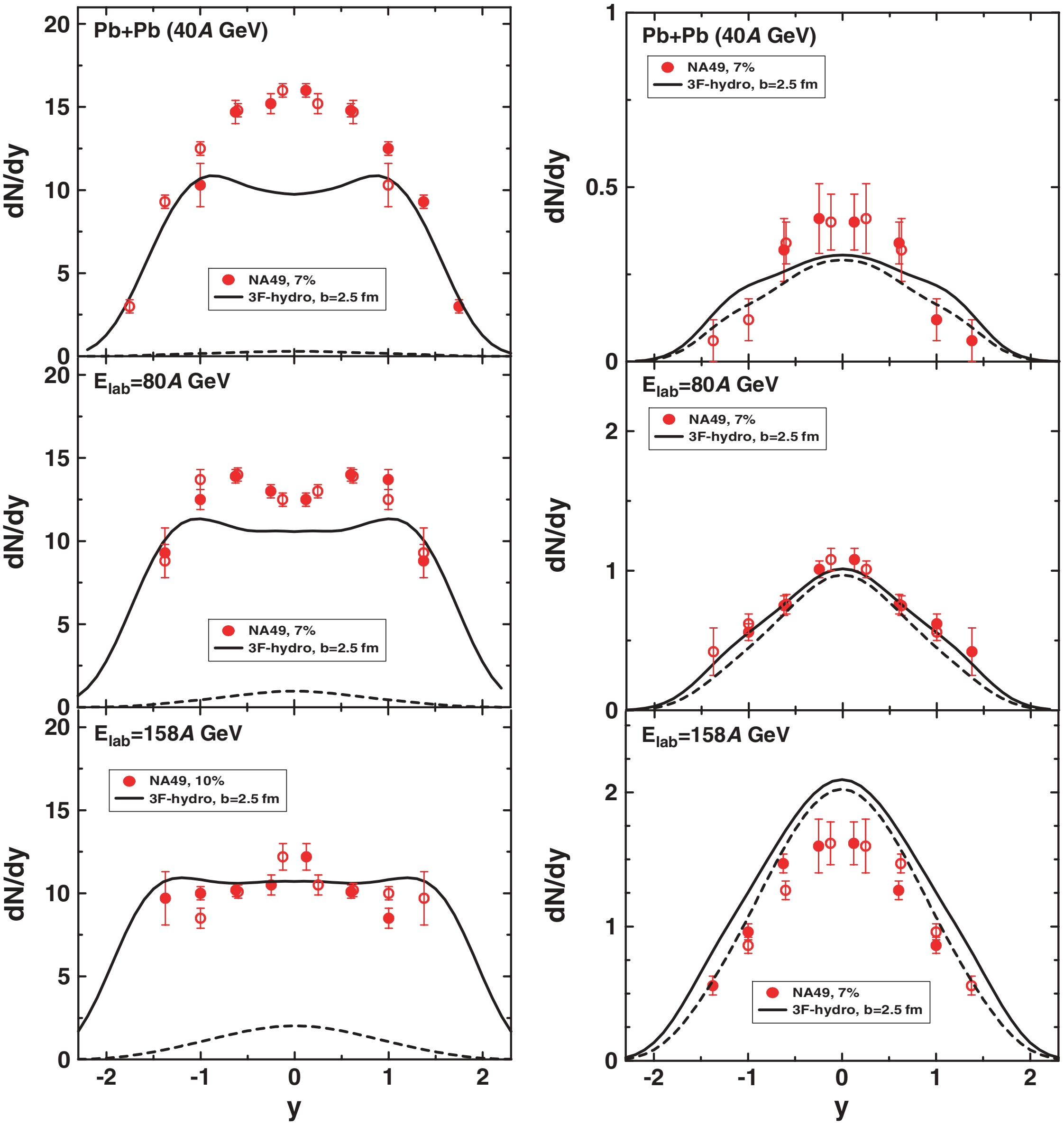

FIG. 10. (Color online) Rapidity spectra of $\Lambda + \Sigma^0$ hyperons (left panel) and $\bar{\Lambda} + \bar{\Sigma}^0$ antihyperons (right panel) from central ($b = 2.5$ fm) Pb+Pb collisions. Solid lines represent results of the three-fluid model. Contributions from the fireball fluid are shown by dashed lines. Preliminary experimental data are taken from Ref. [59]. The percentage indicates the fraction of the total reaction cross section, corresponding to experimentally selected events.

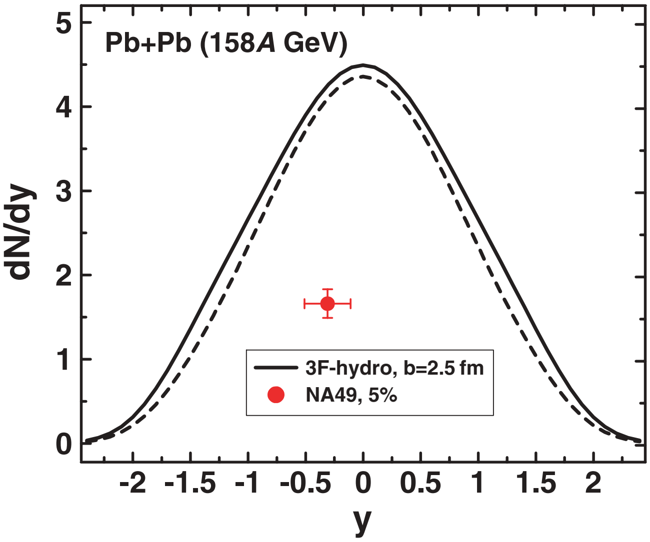

FIG. 11. (Color online) Antiproton rapidity spectrum from central Pb(158*A* GeV)+Pb collisions. Notation is the same as in Fig. 10. Experimental data are taken from Ref. [60].

distinguished in our model, we have estimated the antiproton yield as half of that of antinucleon: $N_{\bar{p}} = \frac{1}{2}N_{\bar{N}}$, assuming that $p\bar{p}$ and $n\bar{n}$ pairs are produced with approximately equal probability. The contributions of weak-decay channels $\bar{\Lambda} \to \bar{N} + \pi$ and $\bar{\Sigma} \to \bar{N} + \pi$ are excluded.

G. Flow

Flow quantities of different types quantify space-momentum correlations of collective motion of the strongly interacting matter. This collective motion is essentially caused by the pressure gradients arising during the evolution of the collision and hence is intimately related to the EOS and, in particular, to a possible phase transitions. A spectacular loss of correlation between the observed particle transverse momenta and the reaction plane, which gives rise to dramatic reduction of the directed flow, has been predicted by Rischke *et al.* [61] in the conventional hydrodynamic model with the bag-model EOS. The subsequent studies showed that the observed signal essentially depends not only on the EOS but also on the collision dynamics [12,15].

The conventional transverse-momentum flow of an *a* species is defined as [62], cf. Eq. (41),

$$\langle p_x^{(a)}\rangle(y) = \frac{\int d^2p_T\, p_x\left(E dN_a/d^3p + \sum_R E d^3N_a^{(R\to a+X)}/d^3p\right)}{\int d^2p_T\left(E dN_a/d^3p + \sum_R E d^3N_a^{(R\to a+X)}/d^3p\right)}, \tag{43}$$

where p_x is the transverse momentum of a particle in the reaction plane, and integration runs over the transverse momentum p_T. The second term in square brackets takes into account the contribution of resonance decays, resulting in *a* production, cf. Appendix B, the sum runs over all relevant resonances *R*.

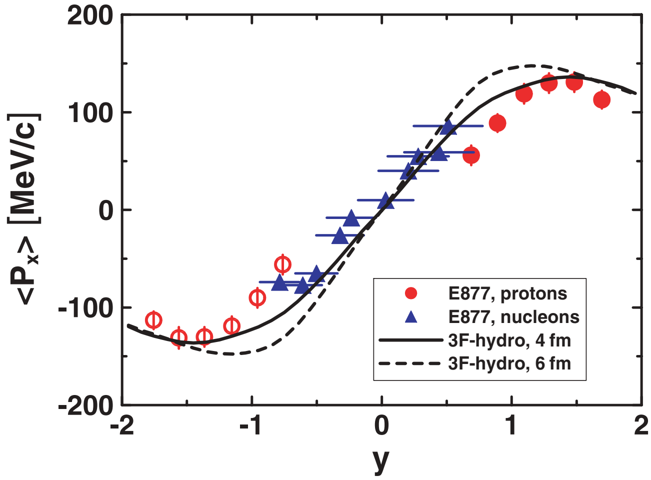

FIG. 12. (Color online) Transverse-momentum flow of nucleons and protons as a function of rapidity for semicentral Au+Au collisions at $E_{\text{lab}} = 10.5A$ GeV. The three-fluid calculations are presented for $b = 4$ fm (solid line) and $b = 6$ fm (dashed line). The data for protons (circles) and all baryons (triangles) are taken from Ref. [63]. Full symbols correspond to measured data, open ones are those reflected with respect to the midrapidity point.

As seen in Fig. 12, the three-fluid model reasonably reproduces a general trend of the baryonic $\langle p_x\rangle(y)$ distribution at $E_{\text{lab}} = 10.5A$ GeV, exhibiting two clear peaks near the target and projectile rapidities. In fact, we compute $\langle p_x\rangle(y)$ of so-called primordial nucleons, which later may coalesce, forming light fragments. In view of this, it is not surprising that agreement with the nucleon $\langle p_x\rangle(y)$ data, which indeed take into account contribution of light nuclear fragments, seems to be better than that with identified-proton data.

At high energies the azimuthal asymmetry is usually characterized by the first and second coefficients of Fourier expansion of the azimuthal-angle dependence of the single-particle distribution function, i.e., by the directed flow $v_1 = \langle\cos\phi\rangle$ and elliptic flow $v_2 = \langle\cos 2\phi\rangle$:

$$v_1^{(a)}(y) = \frac{\int d^2p_T(p_x/p_T)\left(E dN_a/d^3p + \sum_R E d^3N_a^{(R\to a+X)}/d^3p\right)}{\int d^2p_T\left(E dN_a/d^3p + \sum_R E d^3N_a^{(R\to a+X)}/d^3p\right)}, \tag{44}$$

$$v_2^{(a)}(y) = \frac{\int d^2p_T\left[(p_x^2-p_y^2)/p_T^2\right]\left(E dN_a/d^3p + \sum_R E d^3N_a^{(R\to a+X)}/d^3p\right)}{\int d^2p_T\left(E dN_a/d^3p + \sum_R E d^3N_a^{(R\to a+X)}/d^3p\right)}. \tag{45}$$

Examples of the v_1 and v_2 flow for protons and pions at $E_{\text{lab}} = 40A$ and $158A$ GeV are presented in Figs. 13 and 14. The declared experimental percentage of the total reaction cross section, related to the experimental event selection, allows us to estimate the corresponding impact parameter as $b = 5.6$ fm. In view of uncertainty of this estimate and to reveal the model dependence on the impact parameter,

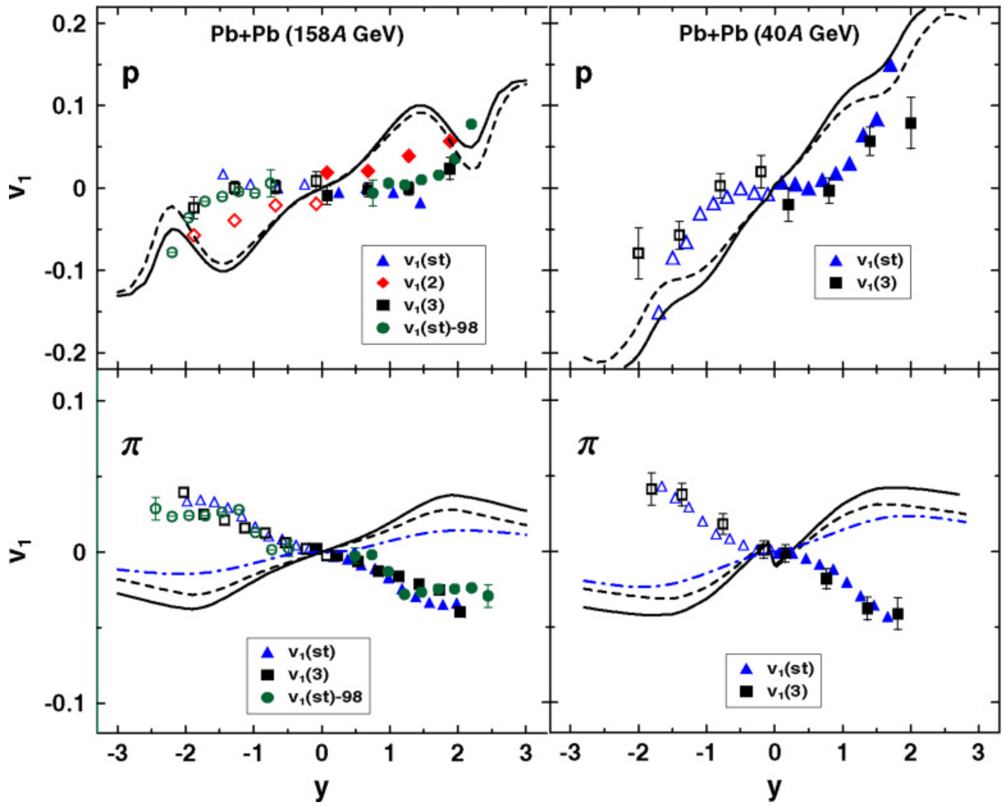

FIG. 13. (Color online) Directed flows of protons (upper panels) and charged pions (lower panels) in semicentral Pb+Pb collisions at $E_{\text{lab}} = 158A$ (right panels) and $40A$ (left panels) GeV as functions of rapidity. The three-fluid calculations are presented for $b = 5.6$ fm (solid line) and $b = 4$ fm (dashed line). The dot-dashed lines show contributions of the fireball fluid. Experimental data are taken from Ref. [64]. These data were obtained by two different experimental procedures: the standard one [$v_{1,2}(st)$] and the method of n-particle correlations [$v_{1,2}(n)$]. Full symbols correspond to measured data, whereas the open symbols are those reflected with respect to the mid rapidity. Updated data of the NA49 Collaboration [65][$v_{1,2}(st) - 98$] with acceptance $0.05 < p_T < 0.35$ GeV/c for pions and $0.6 < p_T < 2.0$ Gev/c for protons, are also shown.

we also show calculations with $b = 4$ fm. Flows of the fireball fluid calculated at $b = 4$ and 5.6 fm are hardly distinguishable. Several sets of data, which noticeably differ from each other, are shown in these figures. The "standard" method [62,66] for evaluating the flow coefficients requires an event-by-event estimate of the reaction plane with which outgoing hadrons correlate. However, this method does not discriminate other sources of correlations, like those because of global momentum conservation, resonance decays, etc. Recently a new method of n-particle correlations has been proposed, that affords getting rid of these nonflow correlations in extracting v_1 and v_2 from genuine azimuthal correlations [67]. Note that only statistical errors are indicated in these figures. The systematic error for protons is 0.005 for v_2 and 0.01 for v_1 at $158A$ GeV, they can be by 50% larger at $40A$ GeV [64].

At these energies the three-fluid v_1 flow significantly differs from the data. Overall, the three-fluid model predicts an essentially stronger directed flow than that experimentally observed. This disagreement cannot be caused by either uncertainties in the impact parameters or application of different methods for measuring the directed flow [64]. Moreover, the calculated pion directed flow closely follows the pattern of the proton one, whereas the pion v_1 data reveal anticorrelation with proton flow. Note that the v_1 flow in the fireball fluid is very weak. Therefore, it is not surprising that pion and proton v_1 are correlated in the three-fluid model, because they reflect the same collective motion of the baryon-rich fluids.

The reasons for this poor reproduction of v_1 can be twofold. Certainly the first reason consists in disregarding the fact that a part of frozen-out particles is "shadowed" by still hydrodynamically evolving matter (cf. discussion in Sec. II D). This shadowing means that frozen-out particles cannot freely propagate through the region still occupied by the hydrodynamically evolved matter but rather get reabsorbed into the hydrodynamic phase [109]. Apparently, the baryon directed flow is less affected by this shadowing. The reason is that the baryon directed flow reveals the collective flow of matter, which is mainly built of baryons as the most abundant and heavy component of the system. This collective flow is mainly formed at the early stage of the reaction. Baryon rescatterings within this earlier-formed collective flow at later (freeze-out) stages do not essentially alter the collective transverse momentum of the matter. At the same time, the

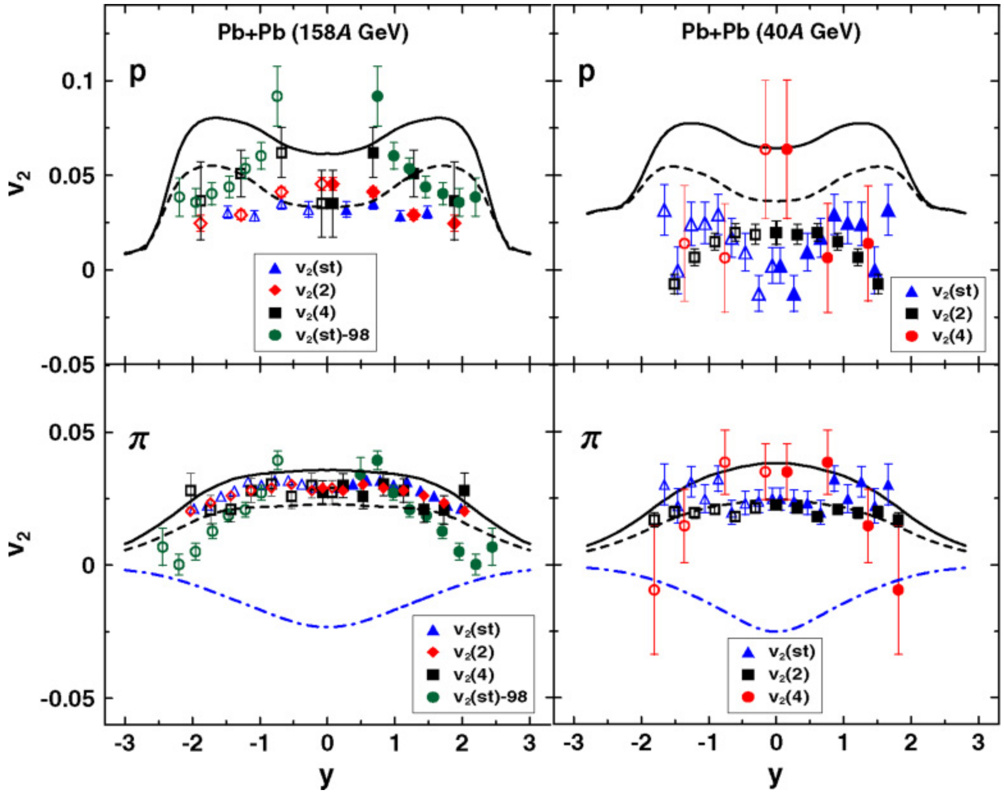

FIG. 14. (Color online) The same as in Fig. 13 but for the elliptic flow.

pions can be much stronger affected by this shadowing, since they are screened by the predominantly baryonic matter, where pions may be essentially decelerated or even absorbed. This can drastically change the pion v_1.

The second possible reason is very probable from our point of view. It could happen that the hadron EOS used in these simulations is too hard, i.e., results in too strong bounce-off of matter. A softer EOS, in particular because of possible phase transition [15,61], would reduce the strength of the proton directed flow in favor of its better reproduction. Then the problem of correlation/anticorrelation with the pion flow would be more delicate, because the shadowing effect could easily change the sign of the pion flow. An additional argument in favor of a softer EOS is the success of microscopic RQMD [68] and UrQMD [69] models, which correspond to essentially softer EOS, because it is closer to that of the gas. These models qualitatively reproduced early measurements of $v_1(y)$ and $v_2(y)$ for both protons and pions at $E_{\mathrm{lab}} = 158A$ GeV. Recently a good microscopic description of the differential flow at 40*A* GeV was also obtained [70].

The calculated elliptic flow of protons (see Fig. 14) is positive ("in plane") and somewhat overestimates experimental points at both incident energies, 40*A* and 158*A* GeV. Though data at 40*A* GeV are still controversial, this overestimate again indicates that the used hadronic EOS is too hard. At the same time, the hydrodynamic pion elliptic flow is in surprisingly good agreement with experimental data of the NA49 Collaboration both in magnitude and shape, exhibiting a shallow minimum at the midrapidity. The elliptic flow v_2 results from the initial spatial asymmetry of noncentral nucleus-nucleus collisions. The overlap lens-shaped geometry of two nearly thermalized nuclei is reproduced correctly in the three-fluid model. As this lens-shaped matter expands, it produces the elliptic flow. Note that mesons emitted from the fireball fluid have negative ("out of plane") v_2 flow.

The earlier pion v_2 data of the NA49 Collaboration, taken at smaller acceptance at the top SPS energy [65], have been already analyzed within hydrodynamic approaches. In the expansion model [71] the Bjorken scaling solution [72] was assumed for longitudinal evolution and 2D hydro was solved numerically for transverse one. In this way, the elliptic flow could be estimated only at the midrapidity point. The full 3D expansion model with postulated initial conditions was applied to the meson elliptic flow by Hirano [73]. In a qualitative agreement with Ref. [71], it was found that ρ-meson decays result in almost vanishing azimuthal anisotropy of pions near the midrapidity. Let us remind that decays of all relevant resonances are taken into account in our model.

Recently, collective flows in heavy-ion collisions from AGS to SPS energies were systematically studied in a transport model with various assumptions on the nuclear mean field [74]. It was found that momentum dependence in the nuclear mean field is of prime importance for the reproduction of the v_1 and v_2 flows. It turned out that generally our results are rather close to those of Ref. [74], if the mean-field momentum dependence is absent. This is precisely the case in our EOS.

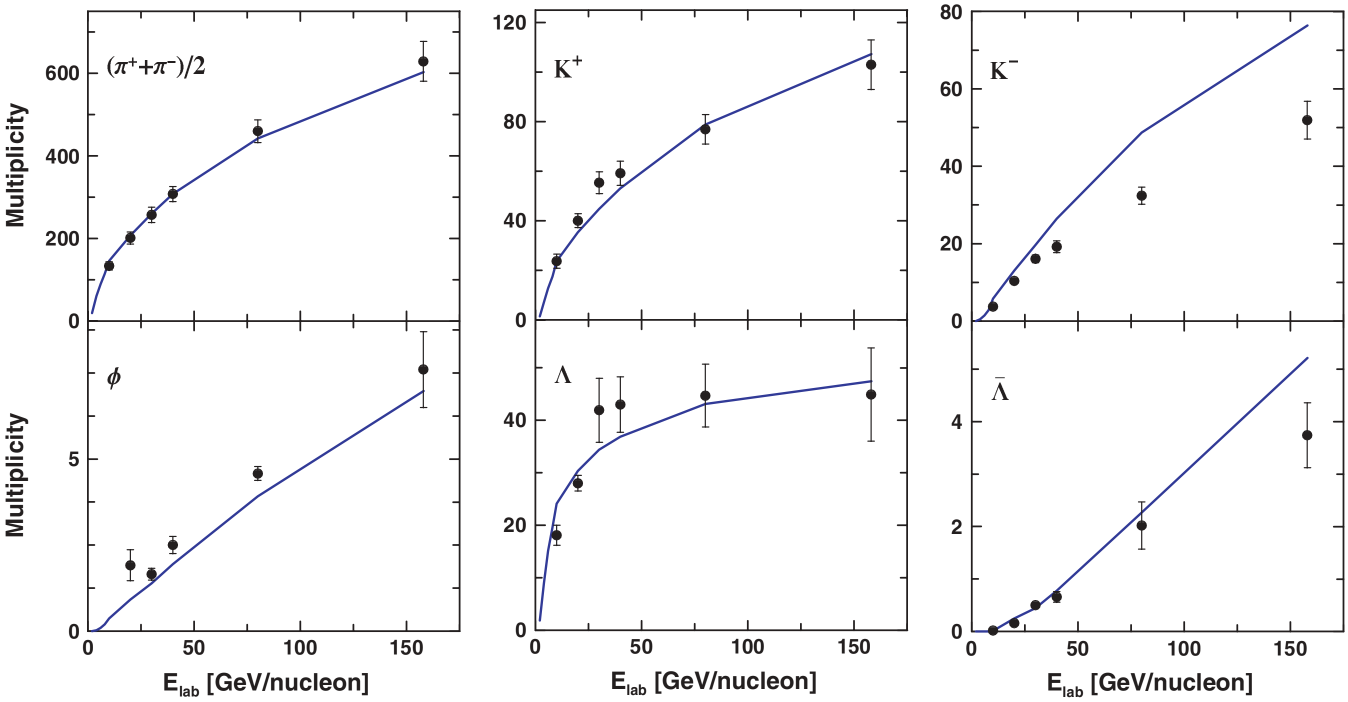

FIG. 15. (Color online) Multiplicities for central Au+Au (at AGS energies) and Pb+Pb (at SPS energies) collisions as functions of the incident energy. Open triangles connected by solid lines represent the three-fluid results. The experimental data (full circles) are taken from Refs. [58,75–85] for SPS energies and from Refs. [86–90] for AGS energies.

It is of interest to note that similarly to our results but in contrast with the experiment, the pion directed flow at $E_{\text{lab}} = 158A$ GeV correlates with the proton v_1 independently of the version chosen for the mean field [74].

H. Multiplicities

Though the quality of reproduction of particle multiplicities was already clear from the above-presented rapidity distributions, we summarize them in this section, as well as present those for hadrons not mentioned above. In Fig. 15, particle multiplicities for central Au+Au (at AGS energies) and Pb+Pb (at SPS energies) collisions as functions of the incident energy are presented and confronted with the experimental data. The experimental data are taken from Refs. [58,75–85] for SPS energies and from Refs. [86–90] for AGS energies. These data are presented as they were summarized in Ref. [91], where they were scaled to the same 5% experimental trigger. Because of this reduction to the same 5% trigger, all the simulations were performed at the same central impact parameters corresponding to this trigger: $b = 2$ fm for Au+Au and $b = 2.5$ fm for Pb+Pb. Corrections for feeddown from weak decays (mostly Ξ^-, Ξ^0 and their antiparticles) were not applied in the original published data. They were, however, estimated to be 6% for Λ and 12% for $\bar{\Lambda}$ [76]. Based on this estimate the Λ and $\bar{\Lambda}$ yields given in Ref. [91] were reduced by 6 and 12%, respectively. This also complies with conditions of our simulations.

We compare our calculated pion multiplicities with the experimental results for half-sum of those for π^+ and π^-, because the model does not distinguish the isospin of particles. Note that the pion multiplicities were fitted by means of the freeze-out parameter and the formation time of the fireball fluid, whereas all other multiplicities are already predictions of the model. As seen, the model reasonably reproduces the energy dependence of various multiplicities, except that for K^-. The latter is strange, especially in view of that even the rare-channel particles, such as ϕ and $\bar{\Lambda}$, are reasonably reproduced without any additional tuning. Probably, a kind of post-hydro kinetic evolution, similar to that performed in Ref. [22], is required for a proper reproduction of the K^- multiplicity. Indeed, cross sections of the reactions $\bar{K}N \to \pi\Lambda$ and $\bar{K}N \to \pi\Sigma$ are very high at low relative momenta [2]. The first reaction transforms a part of K^- into Λ. The resulting Λ enrichment would not contradict to data, becasue the NA57 data for the Λ production [92] are certainly above the NA49 data presented in Fig. 15. The second reaction results in a loss of strangeness because of the weak decay $\Sigma^\pm \to N\pi$. In fact, this is the dominant channel for the $\bar{K}$ absorption on nucleons at low energies. In our model such a post-hydro evolution is absent. It is worthwhile to note that the statistical-model fit of the data also overestimate K^- multiplicities at the SPS energies [93].

At comparatively low incident energies $E_{\text{lab}} < 10A$ GeV, the grand canonical treatment of the strangeness production, used in the three-fluid model, becomes poorly applicable. Therefore, we do not present the three-fluid predictions at these energies. At energies $E_{\text{lab}} = (30\text{–}40)A$ GeV the observed

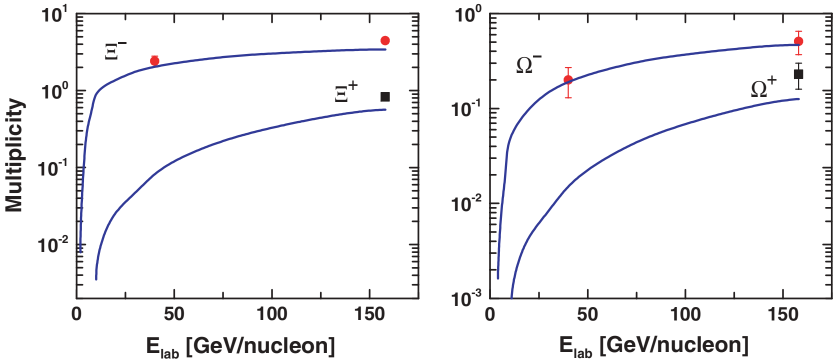

FIG. 16. (Color online) The same as in Fig. 15 but for multiplicities of multistrange hyperons. The experimental data are taken from Refs. [80,94,95]: full circles for hyperons and full squares for antihyperons.

multiplicities of K^+ and Λ are certainly above the smooth curve predicted by the three-fluid model. This correlates with already above observed fact (see Figs. 10 and 14) that agreement with data in this energy region is certainly worse than at other energies.

The excitation functions for production of multistrange hyperons, Ξ and Ω, and the corresponding antihyperons are presented in Fig. 16. In Ref. [80], Ω^- and Ω^+ were not separated at $E_{\text{lab}} = 40A$ GeV. Because of that their total yield is plotted as Ω^-, because the yield of Ω^+ antihyperons is much lower than that of Ω^-. It is seen that calculated multiplicities of multistrange hyperons are also in a reasonable agreement with the available data. Note that these yields are strongly underpredicted in the UrQMD model [80].

IV. GLOBAL EVOLUTION OF NUCLEAR COLLISIONS

In the preceding section, it was shown that the three-fluid hydrodynamic model with the simplest, purely hadronic EOS is able to reasonably reproduce a great body of experimental data on relativistic heavyion collisions. The considered observables characterize a state of the colliding system at the freeze-out stage. With thus fixed parameters of the model, it is possible to address the question of global evolution of nuclear collisions, e.g., the values of baryon and energy densities achieved in the course of them. An important question also is how long and in which volume these achieved values survive. Dynamics of heavy-ion collisions at different bombarding energies are illustrated in Fig. 17. The shown baryon and energy densities are averaged over the whole space occupied by fluids

$$\langle n_B \rangle = \int d^3x n_B W(x) \Big/ \int d^3x W(x), \tag{46}$$

$$\langle \varepsilon \rangle = \int d^3x \varepsilon W(x) \Big/ \int d^3x W(x), \tag{47}$$

where ε and n_B are the proper (i.e., in the local rest frame) densities, and the weight function is taken equal to the local proper baryon density $W(x) = n_B(x)$. This weight function was chosen because we are primarily interested here in evolution of dense baryonic matter. The three-fluid nonequilibrium is quite strong at the initial stage of the collision. The mean values of ε and n_B are calculated by means of averaging these quantities corresponding to either separate fluids (if their mutual stopping has not occurred) or the unified fluid (if the full stopping has happened). To characterize the degree of stopping, we used the auxiliary function introduced in Eq. (23), which reveals quite a sharp transition between transparency ($\vartheta \simeq 1$) and full stopping ($\vartheta \simeq 0$). This convention has been chosen to map the nonequilibrium configuration in terms of equilibrium quantities, avoiding unphysical contributions of the Lorentz contraction and collective motion into quantities $\langle \varepsilon \rangle$ and $\langle n_B \rangle$. However, these results at early stages of collisions should be

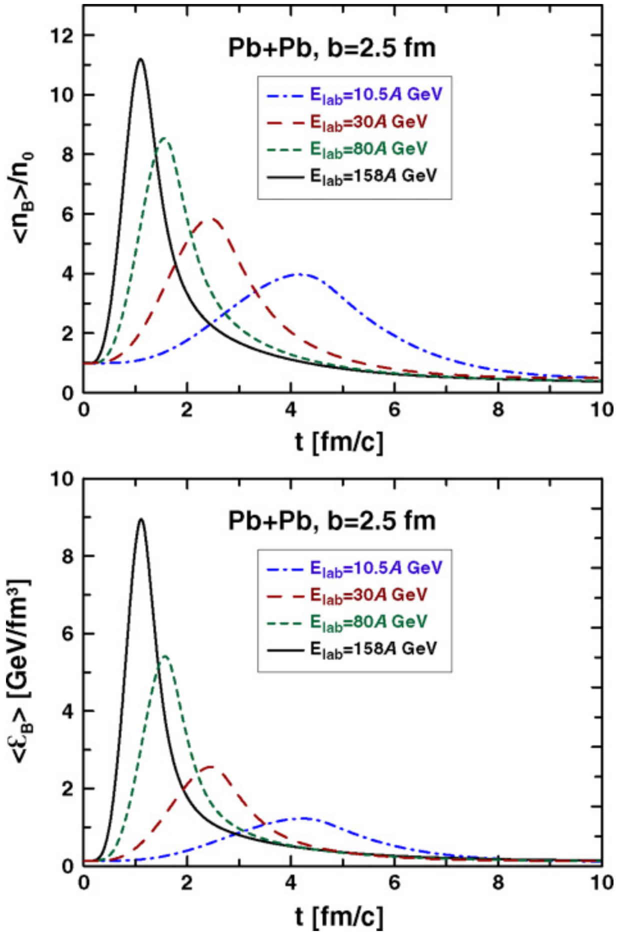

FIG. 17. (Color online) Temporal evolution of average baryon (upper panel) and energy (lower panel) densities for central Pb+Pb collisions within three-fluid model. The time is counted in the c.m. frame of the colliding nuclei.

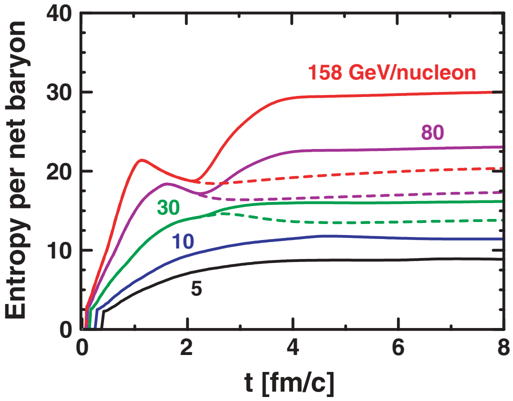

FIG. 18. (Color online) Time evolution of the entropy per baryon number in Pb+Pb central ($b = 2.5$ fm) collisions at various incident energies E_{lab}. The total entropy is displayed by solid lines, while the entropy of baryon-rich subsystem—by dashed lines.

taken with some caution because of certain ambiguities of this mapping convention.

As seen from Fig. 17, the average baryon density $\langle n_B\rangle$ increases quickly reaching a maximum, and then the expansion stage comes. The maximal compression of baryonic matter correlates with maximal overlap of colliding nuclei. Evolution of the average energy density $\langle\varepsilon\rangle$ proceeds in a similar way. Maximal values of baryon and energy densities are high enough, exceeding hypothetic threshold for deconfinement phase transition $\varepsilon \sim 1\,\text{GeV/fm}^3$ even at $E_{\text{lab}} \sim 10A$ GeV. However, these values are slightly lower than those reported in Ref. [1], because here averaging over the whole volume of colliding system is carried out rather than over some fixed central region. Note that local peak values may exceed these average values by a factor of about 2.

To understand the extent of thermalization achieved in the collision process, in Fig. 18 we show the time evolution of the entropy per baryon number (the latter is conserved quantity) in central collisions. These calculations were performed without freeze-out to keep account of the total entropy. We have taken into account the entropy of only formed fireball fluid, because for the unformed part even its definition is ambiguous. Therefore, we deal with an open system, when not all the fireball matter is formed. At the early stage of the collision (until the time instant of complete overlap of nuclei) the entropy quickly rises, which is the evidence of nonequilibrium in the system. After that the total entropy either flatten (at $E_{\text{lab}} < 40A$ GeV) or even slightly drops down (at $E_{\text{lab}} > 40A$ GeV). This entropy flattening naturally means thermalization. The temporal dropping down of the entropy is related to still-continuing production of unformed fireball matter. It starts to form only later, when the entropy starts to rise after the temporal fall. Therefore, at the early stage of the reaction we deal with an open system. The entropy production in the baryon-rich fluids is proportional to the term

$$R = (u_p u_t)(D_P - D_E) - (D_P + D_E),$$

if the fireball fluid is still unformed, cf. Eqs. (6), (7), and (16). This result follows from the standard derivation [96] of hydrodynamic equation for the entropy flow. Therefore, the fall

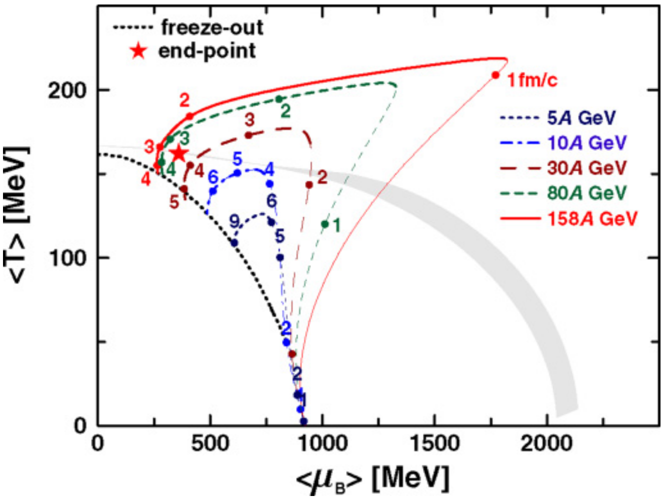

FIG. 19. (Color online) Dynamical trajectories in the (T, μ_B) plane for central Pb+Pb collisions ($b = 2.5$ fm) at various incident energies. Numbers near the dynamical trajectories indicate the evolution time instants in the c.m. frame of the colliding nuclei. Bold parts of trajectories are related to approximately thermalized baryon-rich subsystem, whereas the thin ones—to yet nonequilibrium evolution. The light gray shaded region corresponds to the boundary of the phase transition from the hadronic phase to the QGP, as it was estimated in Ref. [97]. Dotted line is the "experimental" freeze-out curve fitted to observed multiplicities in the approximation of the ideal gas model [98] under condition that the energy per hadron is 1 GeV. The star symbol is the critical end point calculated in Ref. [6].

or rise of the entropy of the baryon-rich fluids depend on the sign of this R. If $R > 0$, the entropy rises. This occurs either at $D_E = 0$, because $(u_p u_t) \geqslant 1$, or when $(u_p u_t) \gg 1$, as it is the case at the initial interpenetration stage. In the region, where the entropy drops down, D_E is still nonzero and $(u_p u_t)$ is not high enough, therefore $R < 0$. In physical terms, the entropy drops down, when the energy-momentum radiation into the fireball fluid $\propto -[(u_p u_t) + 1]D_E$ dominates over the internal heating $\propto [(u_p u_t) - 1]D_P$ of the baryon-rich subsystem.

As seen from Fig. 18, at $E_{\text{lab}} < 40A$ GeV the entropy is approximately conserved already after the colliding nuclei overlap. These overlaps correspond to peak values in Fig. 17 and turning points of the trajectories in Fig. 19. This fact suggests that thermalization in these collisions occurs comparatively early. At higher incident energies, $E_{\text{lab}} > 40A$ GeV, the complete thermalization happens at the comparatively late stage ($t \gtrsim 4$ fm/c), when the fireball fluid gets formed and the entropy approaches the plateau. However, the entropy of the baryon-rich fluids, displayed by dashed lines in Fig. 18, slowly changes already after the complete overlap of nuclei. It remains constant within 10%. This baryon-rich subsystem can be considered as an approximately thermalized fluid still interacting with a "bath" of the fireball matter. Therefore, this overlap time can be approximately taken as a time of equilibration in the baryon-rich subsystem at all considered here incident energies.

Based on the EOS used in simulations, the n_B and ε densities can be recalculated in the temperature-chemical-potential (T, μ_B) representation and displayed in the conventional way as dynamic trajectories in the (T, μ_B) plane, see Fig. 19. In view of the above discussion, we display approximately equilibrium (for the baryon-rich subsystem) parts of the trajectories by bold lines, whereas those yet nonequilibrium–by thin lines, just to keep track of the system evolution. As seen, the compression stage is rather short. For example, at $E_{\rm lab} = 158A$ GeV the maximal values of $\langle T\rangle$ and $\langle \mu_B\rangle$ are reached during the time of about 1 fm/c. After that a comparatively fast expansion, accompanied by rather slow cooling, starts. At the incident energy of $\approx 30A$ GeV, the dynamical trajectory passes near the critical endpoint [6], where the order of the deconfinement phase transition is changed. In fact, the trajectories in the (T, μ_B) plane strongly depend on the used EOS, even if they originate from the same (n_B, ε) initial state. Therefore, this should be taken only as a rough estimate of the relevant incident energy, because the EOS of the hydro simulations has not involved any QGP phase transition at all. The boundary of the phase transition from the hadronic phase to the QGP, estimated in Ref. [97] (light-gray shaded region Fig. 19), is displayed just to remind one what may happen in this thermodynamic domain, if a EOS involves the phase transition. However, this trajectory representation is not quite informative because of the following reason. In addition to the uncertainties of mapping of nonequilibrium on equilibrium above discussed, the displayed time instants correspond to the c.m. frame of colliding nuclei and hence are noninvariant. Therefore, Fig. 19 does not tell us (in invariant way) how long the dense matter survives and in which volume.

The way to overcome the above difficulties was proposed in Ref. [1]. It consists in calculation of an invariant four-volume V_4 in which a quantity q exceeds a given value Q

$$V_4(Q) = \int d^4x \, \Theta\,(q - Q). \tag{48}$$

This quantity provides a Lorentz invariant measure of the space-time region, where the quantity q keeps high value $q \geqslant Q$. In Fig. 20 this four-volume is shown for two cases: $q = n_B^{(\rm eq.)}$ and $q = n_B^{(\rm noneq.)}$. The first case corresponds to the four-volume summed only over those regions, where full stopping [i.e., $\vartheta \simeq 0$ in terms of Eq. (23)] has occurred and thermalized n_B exceeds certain value, whereas in the second case the four-volume is summed over all regions [i.e., similarly to that in Eq. (46)], including those where stopping has not occurred. As seen, for production of the matter with comparatively high densities ($n_B > 4n_0$), there are certain preferable incident energies, that facilitate attainment of the largest four-volume. In particular, incident energies (10–40)A GeV, planned at the new GSI facility, are favorable for production of equilibrated matter with baryon densities higher than $6n_0$. This conjecture is heavily based on the hadronic EOS used. However, we expect that it is not too far from the truth, because we fairly well reproduced the observed stopping power, which is of prime relevance to the achieved compression. To get an impression of the scale of the corresponding four-volume, we draw a short-dashed line presenting the four-volume $\Delta t \times \pi R^2 \times 2R/\gamma_{\rm c.m.}$ composed of Lorentz-contracted cylindrical space volume of radius $R = 4$ fm and time interval $\Delta t = 3$ fm/c, here $\gamma_{\rm c.m.}$ is the γ factor of colliding nuclei in their c.m. frame. It is of interest that the fall-off of the invariant V_4 is defined by this γ factor.

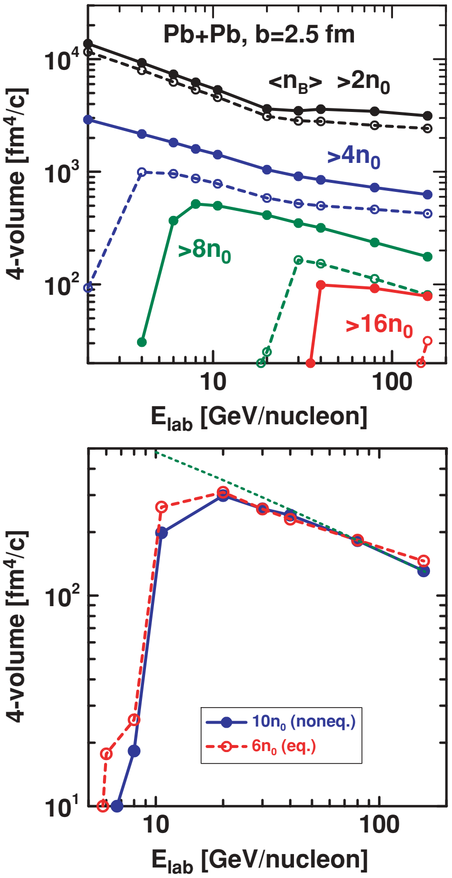

FIG. 20. (Color online) Invariant four-volume corresponding to conditions on $n_B^{(\rm noneq.)}$ (solid lines) and on $n_B^{(\rm eq.)}$ (long-dashed lines) for central Pb+Pb collisions as function of the incident energy. The dotted line on the lower panel is the four-volume $\Delta t \times \pi R^2 \times 2R/\gamma_{\rm c.m.}$ with $R = 4$ fm, $\Delta t = 3$ fm/c (see the text).

V. DISCUSSION AND CONCLUSIONS

In this article we have presented an extension of the three-fluid model for simulating heavy-ion collisions in the range of incident energies between few and about 200A GeV. In addition to two baryon-rich fluids, which constitute the two-fluid model, the baryon-free fireball fluid of newly produced particles with delayed evolution is incorporated. This delay is governed by a formation time, during which the fireball fluid neither thermalizes nor interacts with the baryon-rich fluids. After the formation, it thermalizes and comes into interaction with the baryon-rich fluids. This interaction is estimated from elementary pion-nucleon cross sections.

The hydrodynamic treatment of heavy-ion collisions is an alternative to kinetic simulations. The hydrodynamic approach has certain advantages and disadvantages. Lacking the microscopic feature of kinetic simulations, it overcomes their basic assumption, i.e., the assumption of binary collisions, which is quite unrealistic in dense matter. It directly addresses the nuclear EOS that is of prime interest in heavy-ion research.

Naturally, we have to pay for these pleasant features of hydrodynamics: The treatment assumes that the nonequilibrium stage of the collision can be described by the three-fluid approximation.

Taking advantage of the modern computers, substantial work has been also done on improvement of numerics of the model. In particular, it was found that the numerical diffusion of the computation scheme should be as much as possible avoided to get reliable results in hydro simulations. To avoid the numerical diffusion the parameters of the scheme should be carefully optimized, as it is described in Appendix A.

The main unknowns of the present simulations can be briefly summarized as follows: the equation of state and "cross sections." The EOS is an external input to the calculation and thus can be varied. Our goal is to find an EOS that in the best way reproduces *the largest body of available observables*. The "cross sections" are equally important. They determine friction forces between fluids and hence the nuclear stopping power. At present we have at our disposal only a rough estimate of the friction forces (cf. Ref. [29] for the friction of baryon-rich fluids and Sec.II C for the friction with the fireball). Therefore, we have to fit the friction forces to the stopping power observed in proton rapidity distributions.

In this article we use a purely hadronic scenario in our simulations. This means a very simple EOS [46], constructed under the requirement that it reproduces saturation of the cold nuclear matter. This EOS is a natural reference point for any other more elaborate EOS. We have found out that the original friction between baryon-rich fluids, incorporated in the model accordingly to estimate of Ref. [29], is evidently insufficient to reproduce observable stopping of nuclear matter. Therefore, the original friction was enhanced by means of the tuning factor ξ_h, cf. Eq. (39), which is plotted in Fig. 2. As seen, the enhancement factor turned out to be unexpectedly large. However, it complies with earlier results of the two-fluid model with mean mesonic fields [16]. There it was found out that for the proper reproduction of the data on heavy-ion collisions in the energy range from $0.4A$ to $0.8A$ GeV, where the purely hadronic scenario is certainly applicable, the enhancement by a factor of 3 was required. From this large enhancement we infer that the rough estimate of the friction [24] is really too rough and that further more elaborate microscopic calculations of the friction are required. In doing this at lower energies, we have to rely on pure hadronic effects, e.g., on the concept of the hadron liquid [99] rather than hadron gas. At higher incident energies the friction enhancement could be associated with an indirect manifestation of the onset of the phase transition, although the used EOS does not involve it directly. In Refs. [100–102] it was argued that just above the critical temperature, the quark-gluon system is still a strongly interacting matter rather than a gas of perturbative partons. This strong interaction anomalously enhances interaction cross sections in this phase.

With this simple hadronic EOS we have succeeded in reasonably reproducing a great body of experimental data in the incident energy range $E_{\text{lab}} \simeq (1\text{–}160)A$ GeV. The list includes proton and pion rapidity distributions, proton transverse-mass spectra, rapidity distributions of Λ and $\bar{\Lambda}$ hyperons and antiprotons, elliptic flow of protons and pions (with the exception of proton v_2 at $40A$ GeV), multiplicities of pions, Λ and $\bar{\Lambda}$ hyperons, K^+ mesons and ϕ mesons, $\Xi^{\mp}$ and $\Omega^{\mp}$ multistrange hyperons. However, we have also found out certain problems. The calculated yield of K^- is approximately a factor of 1.5 higher than that in the experiment. We have also failed to describe directed transverse flow of protons and pion at $E_{\text{lab}} \geqslant 40A$ GeV. This especially concerns pions, v_1 of which experimentally anticorrelate with that of protons, while it correlates in our calculations. This failure apparently indicates that the used EOS is too hard and thereby leaves room for a phase transition, which always makes the EOS softer.

The used hadronic EOS allows modifications relating to different incompressibilities (K) of the nuclear matter. We performed simulations with soft ($K = 210$ and 235 MeV) and hard ($K = 380$ MeV) EOSs. We have found out that the data certainly prefer soft EOS. All the calculations presented in this article correspond to $K = 210$ MeV.

The analysis of the global evolution of central Pb+Pb collisions with present hadronic scenario shows in particular that incident energies $(10\text{–}40)A$ GeV, planned at the new GSI facility, are favorable for production of equilibrated matter with baryon densities 6 times higher than the normal nuclear density. This conclusion is heavily based on the simple hadronic EOS used in our calculations. However, we expect that it is not too far from the truth, because we fairly well reproduced the observed stopping power, which is of prime relevance to the achieved compression. Moreover, in this energy range dynamical (T, μ_B) trajectories of nuclear collisions pass in the vicinity of the critical end point, as it is estimated in Ref. [6]. Note that the presently used EOS does not involve any phase transition. In view of the latter, it is intriguing that discrepancies of the present hadronic scenario with the data (i.e., in the form of the Λ rapidity distribution, proton and pion v_1 and v_2, and strangeness production) are most clearly seen at incident energies about $40A$ GeV.

Our present experience shows that to conclude on the relevance of a particular EOS the whole available set of data should be analyzed in a wide incident energy range with the same fixed parameters of the model. This is one of the main conclusions of our article. Indeed, any particular piece of data can be apparently fitted by means of fine tuning of these parameters, whereas to fit the whole set of them, one needs a really good EOS. In the present article we analyzed various data only fragmentarily, just to fit the parameters and to give an overview of the resulting predictions, because the framework of a single article does not allow us to do more. Our preliminary conclusion is that the considered hadronic EOS is not perfect at higher incident energies $E_{\text{lab}} \gtrsim 20A$ GeV because of the above-mentioned problems. Detailed analysis of particular pieces of available data will be reported in forthcoming articles. We are also going to extend our analysis to other EOSs involving phase transition to the QGP. The source code of the three-fluid model is publically available on the Web page http://theory.gsi.de/~mfd/. Free downloads of the code are available from there. Brief instructions on how to run this code are also given on this page.

ACKNOWLEDGMENTS

We are grateful to E. L. Bratkovskaya, B. Friman, M. Gadzicki, G. L. Melkumov, I. N. Mishustin, J. Randrup, L. M. Satarov, V. V. Skokov, and D. N. Voskresensky for fruitful discussions. We are especially grateful to D.H. Rischke for careful reading of the manuscript and making numerous useful comments. This work was supported in part by the Deutsche Forschungsgemeinschaft (DFG project 436 RUS 113/558/0-3), the Russian Foundation for Basic Research (RFBR grant 06-02-04001 NNIO_a), Russian Minpromnauki (grant NS-1885.2003.2).

APPENDIX A: NUMERICS

The relativistic 3D code for the above described three-fluid model was constructed by means of modifying the existing two-fluid 3D code of Refs. [10,11]. The numeric scheme of the code is based on the modified particle-in-cell method [42, 43], which is an extension of the scheme first applied in Los Alamos [44]. Taking advantage of modern computers, we have comprehensively tested this numeric scheme to find optimal parameters of the calculation.

In the particle-in-cell method the matter is represented by an ensemble of Lagrangian test particles. They are used for calculation of the drift transfer of the baryonic charge, energy, and momentum. In the present scheme the test particle has a size of the cell. Therefore, when a single test particle is moved on the grid, it changes quantities in eight cells, with which it overlaps. These spatially extended particles make the scheme smoother and hence more stable. The transfer because of pressure gradients, friction between fluids and production of the fireball fluid, is computed on the fixed grid (so called Euler step of the scheme). Simulation is performed in the frame of equal velocities of colliding nuclei. In view of this combined nature of the numerical scheme there are parameters of the test particles and the grid, which are summarized in the Table II.

The basic scale of the numerical scheme is chosen along the x direction (the transverse direction in the reaction plane). According to the preset number of cells in the x direction, L_x, the maximal impact parameter $b_{\max}$, which is foreseen for the simulation, and number cells free of the matter, reserved for transverse expansion, L_x^{free}, the Δx step of the grid is determined as follows

$$\Delta x = \max\{2R_t; R_p + R_t + b_{\max}\} \big/ \left(L_x - L_x^{\text{free}}\right),$$

where R_p and R_t are radii of the projectile and target nuclei, respectively [110]. Another transverse step Δy (in the out-of-reaction-plane direction) is taken equal to Δx: $\Delta y = \Delta x$. Δz and Δt are determined by means of preset ratios $\Delta x/\Delta t$ and $\Delta x/\Delta z$. The preset numbers of cells in the y and z directions (L_y and L_z) are used to finally define the size of the grid. The simulation takes place only in the semispace $y > 0$ because of the symmetry of the system with respect to the reaction plane. The number of baryon-rich test particles ($N_{\text{tot}}^{\text{bar}} = N_{\text{projectile}}^{\text{bar}} + N_{\text{target}}^{\text{bar}}$) is specified at the initialization step of the simulation. As for produced baryon-free fluid, the actual total number of corresponding test particles depends on the incident energy, the size of the cell and the number of produced fireball test particles per cell and per time step (N_f) and is determined only on the completion of the simulation. The maximal total number of baryon-free test particles $N_{\text{tot}}^{\text{fire}}$ should be larger than the actual total number. $N_{\text{tot}}^{\text{fire}}$ is used to reserve memory for baryon-free test particles.

To get reasonable accuracy in the simulation, the following basic requirements should be met:

(i) The grid should be extended enough to prevent escaping the matter beyond this region before it gets frozen out.
(ii) The grid in the beam (z) direction should be fine enough for a reasonable description of the matter of initially Lorentz-contracted nuclei. From the practical point of view, it is desirable to have more than 30 cells on the Lorentz-contracted nuclear diameter.
(iii) The well-known Courant-Friedrichs-Lewy criterion states that the ratios of the space-grid steps to the time step (e.g., $\Delta x/\Delta t$) should be larger than 1 to have a consistent and stable algorithm for solving hyperbolic partial-differential equations. To avoid numerical diffusion, this ratios should be taken optimal. As it was found in one-dimensional simulations of exactly solvable problems [43], the optimal range of these ratios is $2.5 < \Delta x/\Delta t < 6$ with the preferable $\Delta x/\Delta t \simeq 3.5$, minimizing the numerical diffusion. This fact dictates the choice of equal-step grid in all directions ($\Delta x : \Delta y : \Delta z = 1:1:1$), in spite of Lorentz-contraction of incident nuclei, which is quite strong at high energies. This choice makes the scheme isotropic with respect to the numerical diffusion. However, in view of (i) and (ii) requirements it makes the grid too fine in the transverse directions and thus results in high memory consumption. The need of the equal-step grid in all directions for relativistic hydrodynamic computations within conventional one-fluid model was pointed out in Ref. [45]. As it was demontrated there, the matter transport becomes even acausal if this condition is strongly violated.
(iv) The number of test particles per cell should be high enough to avoid large numerical fluctuations in drift transfer. In practice, this means that this number should be not less than 3 during the whole evolution of expanding matter, till its complete freeze-out.

TABLE II. Basic parameters of the numeric scheme used for simulations of Au+Au and Pb+Pb collisions at various incident energies E_{lab}.

E_{lab}, A GeV	$1 \div 10$	$20 \div 158^*$	158^{**}
L_x	150	320	320
L_y	60	130	130
L_z	240	820	820
L_x^{free}	5	43	43
$\Delta x/\Delta t$	3.5	3.5	4
$\Delta x/\Delta z$	1	1	1.2
$N_{\text{tot}}^{\text{bar}}$	2×10^6	15×10^6	15×10^6
N_f	2	2	2
$N_{\text{tot}}^{\text{fire}}$	3×10^6	25×10^6	25×10^6

The final check of these requirements is possible only upon completion of the simulation. The Table II presents the optimized set of parameters for calculations of Au+Au and Pb+Pb collisions at various incident energies. This set was determined by multiple test runs of the code. The reaction Pb+Pb at $E_{\rm lab} = 158A$ GeV is the most memory and time consuming case considered in simulations. To completely fulfill the requirement (iii) in this calculation we need 8 GB of memory for the central collision (see column $20 \div 158^*$ in Table II). To comply with memory restrictions, we still had to take slightly unequal steps in different directions: $\Delta x : \Delta y : \Delta z = 1.2 : 1.2 : 1$, $\Delta x/\Delta t = \Delta y/\Delta t = 4$ and $\Delta z/\Delta t = 3.3$ (see column 158^{**} in Table II), for noncentral Pb+Pb collisions at $E_{\rm lab} = 158A$ GeV.

The freeze-out criterion [Eq. (30)] is checked at the Lagrangian step of the scheme. It is checked in the cells, which overlap with the considered test particle. As mentioned above, the test particle has a volume of the cell. Therefore, each test particle overlap with eight cells. If the freeze-out criterion is met in *all these cells*, this test particle is frozen out and removed from further hydrodynamic evolution. Thus, the frozen-out test particles are those droplets mentioned in Eq. (33) for the spectrum of observable hadrons. Precisely because of this extended checking in eight cells, the actual freeze-out energy density [111] $\varepsilon_{\rm frz}$ participating in the freeze-out criterion (30) differs from that used in the code $\varepsilon_{\rm frz}^{\rm code}$. According to our estimate, the actual freeze-out energy density $\varepsilon_{\rm frz}$ is approximately twice as lower than $\varepsilon_{\rm frz}^{\rm code}$. This estimate was checked numerically. The reason behind this extended checking in eight cells is as follows. Had we checked the criterion only in a single cell, where the test particle is located, we would prevent any hydrodynamic expansion of the system. Indeed, if the matter, during its expansion, starts to fill in a cell, which was empty before that, it occupies less than 1/3 of this cell during the single time step, because the time step should be less than the space step (cf. $\Delta x/\Delta t = 3.5$) for this numerical scheme. Then, all the densities in this newly filled-in cell are quite low at this time step. Therefore, the freeze-out criterion is certainly fulfilled in this cell. Had we confined ourselves to checking only this cell, we would immediately freeze the matter in this cell out, thus preventing hydrodynamic expansion of the matter.

To avoid formation of bubbles of frozen out matter inside the dense environment, we introduced additional criterion of the freeze-out: at least one of the above discussed cells should be empty, i.e., contain no test particles [112]. This additional criterion means that the analyzed test particle is located near the surface of the system, provided, of course, that the number of test particles per cell is large enough [cf. condition (iv)], which excludes origination of such empty cells because of fluctuations.

APPENDIX B: RESONANCE DECAYS

1. General consideration

Contribution of resonance decays into stable particle spectra has been studied long ago [103] and later analyzed in more detail [104]. To make the article self-contained, we briefly present here formulas for these decays, which in fact are the same as those in Refs. [103,104] but differ from those in presentation, which, from our point of view, is advantageous for numerical realizations.

Consider a hadronic resonance R with degeneracy factor g_R and a spectral function $A_R(s)$, where s is the resonance mass squared, which decays into n particles

$$R \to 1 + 2 + \cdots + n$$

of masses $m_1, m_2, \ldots, m_n$, through a Jth channel of its decay with a branching ratio b_J. Then the distribution of the "1" particle, resulting from this decay, is as follows

$$\begin{aligned}\left(E_1 \frac{d^3 N_1^{(R\to 1+2+\cdots+n)}}{d^3 p_1}\right)_J &= b_J \int_{(\sum_{i=1}^n m_i)^2}^{\infty} ds\, A_R(s) \int \frac{d^3 p_R}{E_R} \left[E_R \frac{d^3 N_R(s, p_R)}{d^3 p_R}\right] \\ &\quad \times \left[E_1 \frac{d^3 \Gamma_1^{(R\to 1+2+\cdots+n)}(s, p_R, p_1)}{d^3 p_1}\right]. \qquad \text{(B1)}\end{aligned}$$

Here, the distribution of the R resonance, produced by the hydrodynamic computation, is

$$E_R \frac{d^3 N_R(s, p_R)}{d^3 p_R} = \frac{g_R V}{(2\pi)^3} \frac{u p_R}{\exp[\beta(u p_R - \mu_R)] \pm 1}, \qquad \text{(B2)}$$

where V is a small proper (i.e., in the rest frame) volume of the fluid element, g_R is degeneracy of the R resonance, u is the hydrodynamic four-velocity, β is the inverse temperature, μ_R is the chemical potential, p_R is the four-momentum of the R resonance, $s = p_R^2$, the upper (lower) sign in this expression corresponds to baryonic (mesonic) resonances. The distribution of the "1" particle, resulting from decay of a single R resonance, is expressed as follows:

$$\begin{aligned}E_1 \frac{d^3 \Gamma_1^{(R\to 1+2+\cdots+n)}(s, p_R, p_1)}{d^3 p_1} &= \frac{1}{2R_n(s)} \int \left(\prod_{i=2}^n \frac{d^3 p_i}{2E_i}\right) \delta^4 \left(p_R - \sum_{i=1}^n p_i\right) \qquad \text{(B3)}\end{aligned}$$

under assumption that the matrix element of the decay is constant all over the available n-particle phase-space volume [105], which, in its turn, reads

$$R_n(s) = \int \left(\prod_{i=1}^n \frac{d^3 p_i}{2E_i}\right) \delta^4 \left(p_R - \sum_{i=1}^n p_i\right). \qquad \text{(B4)}$$

To obtain the total contribution of the R decay into "1" particle spectrum, we should sum over all J branches of the R decay, in which the "1" particle appears, and take into account that particles identical to "1" can also be among residue particles $2, 3, \ldots, n$

$$E_1 \frac{d^3 N_1^{(R\to 1+X)}}{d^3 p_1} = \sum_J N_1^J \left(E_1 \frac{d^3 N_1^{(R\to 1+2+\cdots+n)}}{d^3 p_1}\right)_J. \qquad \text{(B5)}$$

Here N_1^J is the multiplicity of "1" particles in the Jth channel of the R decay. Here and below, $E_R = (s + \mathbf{p}_R^2)^{1/2}$ and $E_i = (m_i^2 + \mathbf{p}_i^2)^{1/2}$.

Fortunately, the the major part of integrations involved in Eqs. (B1) and (B3) can be performed analytically. We explicitly present results only for two-particle and three-particle decays, which are dominant for resonances under consideration.

2. Two-particle decays

The result for a two-particle decay of a R resonance is as follows:

$$\begin{aligned}\left(E_1\frac{d^3N_1^{(R\to 1+2)}}{d^3p_1}\right)_J &= b_J\frac{g_RV}{(4\pi)^2}\frac{1}{\left[(up_1)^2-m_1^2\right]^{1/2}}\\ &\quad\times\int_{(m_1+m_2)^2}^{\infty}ds\,\frac{A_R(s)}{R_2(s)}\sum_{n=1}^{\infty}(\mp 1)^{n-1}\\ &\quad\times\left\{\frac{n\beta E_R+1}{(n\beta)^2}\exp[-n\beta(E_R-\mu_R)]\right\}_{E_R^+}^{E_R^-},\end{aligned}\tag{B6}$$

where the upper (lower) sign in this expression corresponds to baryonic (mesonic) resonances,

$$R_2(s)=\frac{\pi}{2s}\lambda^{1/2}\left(s,m_1^2,m_2^2\right)\tag{B7}$$

is the two-particle phase-space volume and

$$\begin{aligned}E_R^{\pm} &= \frac{1}{2m_1^2}\left\{\left(s+m_1^2-m_2^2\right)(up_1)\right.\\ &\quad\left.\pm\lambda^{1/2}\left(s,m_1^2,m_2^2\right)\left[(up_1)^2-m_1^2\right]^{1/2}\right\}.\end{aligned}\tag{B8}$$

Here and below

$$\lambda(x,y,z)=(x-y-z)^2-4yz\tag{B9}$$

is the standard kinematic function [105]. To arrive to this result, the following expansion

$$\frac{1}{\exp[\beta(up_R-\mu_R)]\pm 1}=\sum_{n=1}^{\infty}(\mp 1)^{n-1}\exp\{-n\beta(up_R-\mu_R)\}\tag{B10}$$

was used, the advantage of which is that it is rapidly convergent, when $up_R > \mu_R$. The opposite limit, i.e., $up_R < \mu_R$, corresponds to low temperatures and hence hardly contributes to the resonance production. The $n = 1$ term in this expansion, as well in Eq. (B6), corresponds to the classical Jüttner distribution.

3. Three-particle decays

The result for a three-particle decay of a R resonance is as follows:

$$\begin{aligned}\left(E_1\frac{d^3N_1^{(R\to 1+2+3)}}{d^3p_1}\right)_J &= b_J\frac{g_RV}{32\pi}\frac{1}{\left[(up_1)^2-m_1^2\right]^{1/2}}\\ &\times\int_{(m_1+m_2+m_3)^2}^{\infty}ds\,\frac{A_R(s)}{R_3(s)}\int_{\sqrt{s}}^{\infty}dE_R\theta(X^+/X^-)\\ &\times\theta\left[\frac{\left(m_2^2-m_3^2\right)^2-\left(m_2^2+m_3^2\right)X^++\left|m_2^2-m_3^2\right|\sqrt{\lambda^+}}{\left(m_2^2-m_3^2\right)^2-\left(m_2^2+m_3^2\right)X^-+\left|m_2^2-m_3^2\right|\sqrt{\lambda^-}}\right]\\ &\times\theta\left[\frac{-\left(m_2^2+m_3^2\right)+X^++\sqrt{\lambda^+}}{-\left(m_2^2+m_3^2\right)+X^-+\sqrt{\lambda^-}}\right]\\ &\times\left[(\sqrt{\lambda^+}-\sqrt{\lambda^-})+\left|m_2^2-m_3^2\right|\ln\frac{X^+}{X^-}-\left|m_2^2-m_3^2\right|\right.\\ &\times\ln\frac{\left(m_2^2-m_3^2\right)^2-\left(m_2^2+m_3^2\right)X^++\left|m_2^2-m_3^2\right|\sqrt{\lambda^+}}{\left(m_2^2-m_3^2\right)^2-\left(m_2^2+m_3^2\right)X^-+\left|m_2^2-m_3^2\right|\sqrt{\lambda^-}}\\ &\left.-\left(m_2^2+m_3^2\right)\ln\frac{-\left(m_2^2+m_3^2\right)+X^++\sqrt{\lambda^+}}{-\left(m_2^2+m_3^2\right)+X^-+\sqrt{\lambda^-}}\right]\\ &\times\frac{E_R}{\exp[\beta(E_R-\mu_R)]\pm 1}\end{aligned}\tag{B11}$$

where the upper (lower) sign in this expression again corresponds to baryonic (mesonic) resonances,

$$X^+=\min\left(\widetilde{X}^+,X_{\max}\right),\quad X^-=\max\left(\widetilde{X}^-,X_{\min}\right),\tag{B12}$$

$$X_{\max}=\left(s^{1/2}-m_1\right)^2,\quad X_{\min}=(m_2+m_3)^2,\tag{B13}$$

$$\widetilde{X}^{\pm}=s+m_1^2-2E_R\,(up_1)\pm 2\left(E_R^2-s\right)^{1/2}\left[(up_1)^2-m_1^2\right]^{1/2},\tag{B14}$$

$$\lambda^{\pm}=\lambda\left(X^{\pm},m_2^2,m_3^2\right),\tag{B15}$$

$$R_3(s)=\left(\frac{\pi}{2}\right)^2\frac{1}{s}\int_{X_{\min}}^{X_{\max}}\frac{dX}{X}\lambda^{1/2}\left(s,X,m_1^2\right)\lambda^{1/2}\left(X,m_2^2,m_3^2\right),\tag{B16}$$

$\theta(\lambda^+)$, $\theta(\lambda^-)$, etc., are step functions that define the accessible kinematic region.

---

[1] B. Friman, W. Nörenberg, and V. D. Toneev, Eur. Phys. J. A **3**, 165 (1998).

[2] W. Cassing and E. L. Bratkovskaya, Phys. Rep. **308**, 65 (1999).

[3] P. Braun-Munzinger, J. Cleymans, H. Oeschler, and K. Redlich, Nucl. Phys. **A697**, 902 (2002).

[4] M. Gazdzicki *et al.* (NA49 Collaboration), J. Phys. G **30**, S701 (2004).

[5] Conceptual Design Report, *An International Accelerator Facility for Beams of Ions and Antiprotons*, http://www.gsi.de/GSI-Future/cdr/

[6] Z. Fodor and S. D. Katz, J. High Energy Phys. 03 (2002) 14; 04 (2004) 50.

[7] M. Stephanov, K. Rajagopal, and E. Shuryak, Phys. Rev. D **60**, 114028 (1999).

[8] A. A. Amsden, A. S. Goldhaber, F. H. Harlow, and J. R. Nix, Phys. Rev. C **17**, 2080 (1978).

[9] R. B. Clare and D. Strottman, Phys. Rep. **141**, 177 (1986).

[10] I. N. Mishustin, V. N. Russkikh, and L. M. Satarov, Yad. Fiz. **48**, 711 (1988) [Sov. J. Nucl. Phys. **48**, 454 (1988)]; Nucl. Phys. **A494**, 595 (1989).

[11] I. N. Mishustin, V. N. Russkikh, and L. M. Satarov, Yad. Fiz. **54**, 429 (1991) [Sov. J. Nucl. Phys. **54**, 260 (1991)]; in *Relativistic Heavy Ion Physics*, edited by L. P. Csernai and D. D. Strottman, (World Scientific, Singapore, 1991), p. 179.

[12] Yu. B. Ivanov, E. G. Nikonov, W. Nörenberg, V. D. Toneev, and A. A. Shanenko, Heavy Ion Phys. **15**, 117 (2002).

[13] U. Katscher, D. H. Rischke, J. A. Maruhn, W. Greiner, I. N. Mishustin, and L. M. Satarov, Z. Phys. A **346**, 209 (1993); U. Katscher, J. A. Maruhn, W. Greiner, and I. N. Mishustin, *ibid.* **346**, 251 (1993); A. Dumitru, U. Katscher, J. A. Maruhn, H. Stöcker, W. Greiner, and D. H. Rischke, Phys. Rev. C **51**, 2166 (1995); Z. Phys. A **353**, 187 (1995).

[14] J. Brachmann, A. Dumitru, J. A. Maruhn, H. Stöcker, W. Greiner, and D. H. Rischke, Nucl. Phys. **A619**, 391 (1997); A. Dumitru, J. Brachmann, M. Bleicher, J. A. Maruhn, H. Stöcker, and W. Greiner, Heavy Ion Phys. **5**, 357 (1997); M. Reiter, A. Dumitru, J. Brachmann, J. A. Maruhn, H. Stöcker, and W. Greiner, Nucl. Phys. **A643**, 99 (1998); M. Bleicher, M. Reiter, A. Dumitru, J. Brachmann, C. Spieles, S. A. Bass, H. Stöcker, and W. Greiner, Phys. Rev. C **59**, R1844 (1999); J. Brachmann, A. Dumitru, H. Stöcker, and W. Greiner, Eur. Phys. J. A **8**, 549 (2000).

[15] J. Brachmann, S. Soff, A. Dumitru, H. Stöcker, J. A. Maruhn, W. Greiner, L. V. Bravina, and D. H. Rischke, Phys. Rev. C **61**, 024909 (2000).

[16] V. N. Russkikh, Yu. B. Ivanov, Yu. E. Pokrovsky, and P. A. Henning, Nucl. Phys. **A572**, 749 (1994).

[17] Yu. B. Ivanov, V. N. Russkikh, M. Schönhofen, M. Cubero, B. L. Friman, and W. Nörenberg, Z. Phys. A **340**, 385 (1991); Yu. B. Ivanov and V. N. Russkikh, Nucl. Phys. **A580**, 614 (1994); Yad. Fiz. **58**, 2180 (1995) [Phys. At. Nucl. **58**, 2066 (1995)]; **60**, 743 (1997); **60**, 660 (1997); V. N. Russkikh and Yu. B. Ivanov, Nucl. Phys. **A591**, 699 (1995); S. Ayik, Yu. B. Ivanov, V. N. Russkikh, and W. Nörenberg, *ibid.* **A578**, 640 (1994).

[18] Yu. B. Ivanov, I. N. Mishustin, and L. M. Satarov, Nucl. Phys. **A433**, 713 (1985).

[19] Yu. B. Ivanov and L. M. Satarov, Nucl. Phys. **A446**, 727 (1985).

[20] Y. Hama, R. Andrade, F. Grassi, O. Socolowski, T. Kodama, B. Tavares, and S. S. Padula, hep-ph/0510101; V. V. Skokov and V. D. Toneev, Phys. Rev. C **73**, 021902(R) (2006), nucl-th/0601160.

[21] J. Sollfrank, P. Huovinen, M. Kataja, P. V. Ruuskanen, M. Prakash, and R. Venugopalan, Phys. Rev. C **55**, 392 (1997); P. Huovinen, P. V. Ruuskanen, and J. Sollfrank, Nucl. Phys. **A650**, 227 (1999); P. F. Kolb, J. Sollfrank, P. V. Ruuskanen, and U. Heinz, *ibid.* **A661**, 349 (1999); C. Nonaka and S. A. Bass, nucl-th/0510038.

[22] C. M. Hung and E. V. Shuryak, Phys. Rev. Lett. **75**, 4003 (1995); C. M. Hung and E. Shuryak, Phys. Rev. C **57**, 1891 (1998); D. Teaney, J. Lauret, and E. V. Shuryak, nucl-th/0110037.

[23] V. N. Russkikh, Yu. B. Ivanov, E. G. Nikonov, W. Nörenberg, and V. D. Toneev, Phys. At. Nucl. **67**, 199 (2004); V. D. Toneev, Yu. B. Ivanov, E. G. Nikonov, W. Nörenberg, and V. N. Russkikh, Part. Nucl. Lett. **2**, 43 (2005).

[24] S. Bass, *et al.*, Prog. Part. Nucl. Phys. **41**, 225 (1998).

[25] W. Cassing and E. L. Bratkovskaya, Phys. Rep. **308**, 65 (1999).

[26] L. McLerran and R. Venugopalan, Phys. Rev. D **49**, 2233 (1994); **49**, 3352 (1994); F. Gelis, K. Kajantie, and T. Lappi, Phys. Rev. C **71**, 024904 (2005).

[27] I. N. Mishustin and J. I. Kapusta, Phys. Rev. Lett. **88**, 112501 (2002); V. K. Magas, L. P. Csernai, and D. Strottman, Nucl. Phys. **A712**, 167 (2002).

[28] Yu. B. Ivanov, Nucl. Phys. **A474**, 669 (1987).

[29] L. M. Satarov, Yad. Fiz. **52**, 412 (1990) [Sov. J. Nucl. Phys. **52**, 264 (1990)].

[30] Madappa Prakash, Manju Prakash, R. Venugopalan, and G. Welke, Phys. Rep. **227**, 321 (1993).

[31] G. A. Milekhin, Zh. Eksp. Teor. Fiz. **35**, 1185 (1958); Sov. Phys. JETP **35**, 829 (1959); Trudy FIAN **16**, 51 (1961).

[32] F. Cooper and G. Frye, Phys. Rev. D **10**, 186 (1974).

[33] K. A. Bugaev, Nucl. Phys. **A606**, 559 (1996).

[34] J. J. Neumann, B. Lavrenchuk, and G. Fai, Heavy Ion Phys. **5**, 27 (1997).

[35] L. P. Csernai, Z. Lázár, and D. Molnár, Heavy Ion Phys. **5**, 467 (1997).

[36] K. A. Bugaev and M. I. Gorenstein, nucl-th/9903072; K. A. Bugaev, M. I. Gorenstein, and W. Greiner, J. Phys. G **25**, 2147 (1999); Heavy Ion Phys. **10**, 333 (1999).

[37] Cs. Anderlik, L. P. Csernai, F. Grassi, Y. Hama, T. Kodama, Zs. Lázár, and H. Stöcker, Heavy Ion Phys. **9**, 193 (1999).

[38] K. Tamosiūnas and L. P. Csernai, Eur. Phys. J. A **20**, 269 (2004).

[39] E. Molnar, L. P. Csernai, V. K. Magas, A. Nyiri, and K. Tamosiūnas, nucl-th/0503047; E. Molnar, L. P. Csernai, V. K. Magas, Zs. I. Lazar, A. Nyiri, and K. Tamosiūnas, nucl-th/0503048.

[40] F. Grassi, Y. Hama, and T. Kodama, Phys. Lett. **B355**, 9 (1995); Z. Phys. C **73**, 153 (1996); Yu. M. Sinyukov, S. V. Akkelin, and Y. Hama, Phys. Rev. Lett. **89**, 052301 (2002); Y. Hama, T. Kodama, and O. Socolowski, Braz. J. Phys. **35**, 24 (2005).

[41] F. Grassi, Braz. J. Phys. **35**, 52 (2005).

[42] A. S. Roshal and V. N. Russkikh, Yad. Fiz. **33**, 1520 (1981).

[43] V. N. Russkikh, Numerical Methods of Medium Mechanics, (Novosibirsk), **1(18)** 104 (1987).

[44] F. H. Harlow, A. A. Amsden, and J. R. Nix, J. Comput. Phys. **20**, 119 (1976).

[45] B. Waldhauser, D. H. Rischke, U. Katscher, J. A. Maruhn, H. Stöcker, and W. Greiner, Z. Phys. C **54**, 459 (1992).

[46] V. M. Galitsky and I. N. Mishustin, Sov. J. Nucl. Phys. **29**, 181 (1979).

[47] P. Danielewicz, R. Lacey, and W. G. Lynch, Science **298**, 1592 (2002); P. Danielewicz, nucl-th/0512009.

[48] H. Weber, E. L. Bratkovskaya, W. Cassing, and H. Stöcker, Phys. Rev. C **67**, 014904 (2003).

[49] L. Ahle *et al.* (E802 Collaboration), Phys. Rev. C **60**, 064901 (1999).

[50] J. Barrette *et al.* (E877 Collaboration), Phys. Rev. C **62**, 024901 (2000).

[51] B. B. Back *et al.*, (E917 Collaboration), Phys. Rev. Lett. **86** , 1970 (2001).

[52] H. Appelshäuser *et al.* (NA49 Collaboration), Phys. Rev. Lett. **82**, 2471 (1999).

[53] G. E. Cooper (for the NA49 Collaboration) Nucl. Phys. **A661**, 362c (1999).

[54] T. Anticic *et al.* (NA49 Collaboration), Phys. Rev. C **69**, 024902 (2004).
[55] N. Herrmann, Nucl. Phys. **A610**, 49c (1996).
[56] J. L. Klay *et al.* (E895 Collaboration), Phys. Rev. C **68**, 054905 (2003).
[57] M. van Leeuwenet *et al.* (NA49 Collaboration), Nucl. Phys. **A715**, 161c (1999).
[58] S. V. Afanasiev *et al.* (NA49 Collaboration), Phys. Rev. C **66**, 054902 (2002).
[59] T. Anticic *et al.* (NA49 Collaboration), Phys. Rev. Lett. **93**, 022302 (2004).
[60] G. I. Veres *et al.* (NA49 Collaboration), Nucl. Phys. **A661**, 383 (1999).
[61] D. H. Rischke, Y. Pürsün, J. A. Maruhn, H. Stöcker, and W. Greiner, Heavy Ion Phys. **1**, 309 (1995); D. H. Rischke, Nucl. Phys. **A610**, 88c (1996).
[62] P. Danielewicz and G. Odyniec, Phys. Lett. **B157**, 146 (1985).
[63] J. Barrette *et al.* (E877 Collaboration), Phys. Rev. C **56**, 3254 (1997).
[64] C. Alt *et al.* (NA49 Collaboration), Phys. Rev. C **68**, 034903 (2003).
[65] H. Appelshäuser *et al.* (NA49 Collaboration), Phys. Rev. Lett. **80**, 4136 (1998).
[66] A. M. Poskanzer and S. A. Voloshin, Phys. Rev. C **58**, 1671 (1998).
[67] N. Borghini, P. M. Dinh, and J. Y. Ollitrault, Phys. Rev. C **63**, 054906 (2001); **64**, 054901 (2001); **66**, 014905 (2002).
[68] H. Liu, S. Panitkin, and N. Xu, Phys. Rev. C **59** , 348 (1999).
[69] S. Soff, S. A. Bass, M. Bleicher, H. Stoecker, and W. Greiner, nucl-th/9903061.
[70] H. Stöcker, E. L. Bratkovskaya, M. Bleicher, S. Soff, and Z. Zhu, J. Phys. G **31**, S709 (2005).
[71] J. P. Kolb, J. Sollfrank, and U. Heinz, Phys. Lett. **B459**, 667 (1999).
[72] J. D. Bjorken, Phys. Rev. D **27**, 140 (1983).
[73] T. Hirano, Phys. Rev. Lett. **86**, 2754 (2001).
[74] M. Isse, A. Ohnishi, N. Otuka, P. K. Sahu, and Y. Nara, Phys. Rev. C **72**, 064908 (2005).
[75] A. Mischke *et al.*, Nucl. Phys. **A715**, 453 (2003).
[76] T. Anticic *et al.* (NA49 Collaboration), Phys. Rev. Lett. **93**, 022302 (2004).
[77] V. Friese *et al.* (NA49 Collaboration), Nucl. Phys. **A698**, 487 (2002).
[78] S. V. Afanasiev *et al.* (NA49 Collaboration), Phys. Lett. **B538**, 275 (2002).
[79] S. V. Afanasev *et al.* (NA49 Collaboration), Phys. Lett. **B491**, 59 (2000).
[80] C. Alt *et al.* (NA49 Collaboration), Phys. Rev. Lett. **94**, 192301 (2005).
[81] C. Alt *et al.* (NA49 Collaboration), J. Phys. G **30**, S119 (2004).
[82] M. Gazdzicki *et al.* (NA49 Collaboration), J. Phys. G **30**, S701 (2004).
[83] C. Meurer *et al.* (NA49 Collaboration), J. Phys. G **30**, S1325 (2004).
[84] A. Richard *et al.* (NA49 Collaboration), J. Phys. G **31**, S155 (2005).
[85] C. Blume *et al.* (NA49 Collaboration), J. Phys. G **31**, S685 (2005).
[86] L. Ahle *et al.* (E802 Collaboration), Phys. Rev. C **59**, 2173 (1999).
[87] L. Ahle *et al.* (E802 Collaboration), Phys. Rev. C **60**, 044904 (1999).
[88] L. Ahle *et al.* (E802 Collaboration), Phys. Rev. C **60**, 064901 (1999).
[89] S. Albergo *et al.*, Phys. Rev. Lett. **88**, 062301 (2002).
[90] S. Ahmad *et al.*, Phys. Lett. **B382**, 35 (1996).
[91] F. Becattini, M. Gazdzicki, A. Keranen, J. Manninen, and R. Stock, Phys. Rev. C **69**, 024905 (2004).
[92] F. Antinori *et al.* (NA57 Collaboration), Phys. Lett. **B595**, 68 (2004); J. Phys. G **31**, 1345 (2005).
[93] A. Andronic, P. Braun-Munzinger, and J. Stachel, nucl-th/0511071.
[94] S. V. Afanasiev *et al.* (NA49 Collaboration), Phys. Lett. **B538**, 275 (2002).
[95] C. Meurer *et al.* (NA49 Collaboration), J. Phys. G **30**, S1325 (2004).
[96] L. D. Landau and E. M. Lifshitz, *Fluid Mechanics* (Pergamon Press, Oxford, 1979).
[97] V. D. Toneev, E. G. Nikonov, B. Friman, W. Nörenberg, and K. Redlich, Eur. Phys. J. C **32**, 399 (2004).
[98] J. Cleymans and K. Redlich, Phys. Rev. Lett. **81** 5284 (1998).
[99] D. N. Voskresensky, Nucl. Phys. **A774**, 378 (2004).
[100] E. V. Shuryak and I. Zahed, Phys. Rev. C **70**, 021901(R) (2004).
[101] G. E. Brown, Ch.-H. Lee, and M. Rho, hep-ph/0402207.
[102] A. Peshier and W. Cassing, Phys. Rev. Lett. **94**, 172301 (2005).
[103] J. I. Kapusta, Phys. Rev. C **16**, 1493 (1977).
[104] J. Sollfrank, P. Koch, and U. Heinz, Z. Phys. C **52**, 593 (1991).
[105] E. Byckling and K. Kajantie, *Particle Kinematics* (Wiley, London, 1773).

[106] Note that in the mean-field multifluid dynamics [16,17] this problem is overcome.

[107] In fact, the particle emission would create pressure against the emitting surface, if we allow feedback between the frozen-out matter and the still hydrodynamic system, i.e., if some particles from the frozen-out matter return into the hydrodynamic system. This is a long-standing problem of the freeze-out procedure still waiting for its consistent solution.

[108] Note that Σ^0 and $\bar{\Sigma}^0$ suffer the sequence of electromagnetic and weak decays: $\Sigma^0 \to \Lambda\gamma \to N\pi\gamma$.

[109] Of course, the conventional shadowing (of participants by spectators) is automatically taken into account in our calculations: there simply is no emission from our participants into the direction of spectators, because they are not separated by any freeze-out region. Moreover, the "participants" and "spectators" are very approximate terms for different parts of the unified hydrodynamic system.

[110] Here, we assumed that, if colliding nuclei are different, then the larger one is target.

[111] Related to the cell, where the center coordinate of the frozen-out test particle belongs to.

[112] By definition, the cell is empty, if no center coordinate of any test particle belongs to this cell.